

JUNO Sensitivity to Invisible Decay Modes of Neutrons

JUNO collaboration

Angel Abusleme^{6,5} Thomas Adam⁴⁵ Kai Adamowicz⁴⁸ Shakeel Ahmad⁶⁶ Rizwan Ahmed⁶⁶ Sebastiano Aiello⁵⁵ Fengpeng An²¹ Qi An²³ Giuseppe Andronico⁵⁵ Nikolay Anfimov⁶⁷ Vito Antonelli⁵⁷ Tatiana Antoshkina⁶⁷ João Pedro Athayde Marcondes de André⁴⁵ Didier Auguste⁴³ Weidong Bai²¹ Nikita Balashov⁶⁷ Wander Baldini⁵⁶ Andrea Barresi⁵⁸ Davide Basilico⁵⁷ Eric Baussan⁴⁵ Marco Bellato⁶⁰ Marco Beretta⁵⁷ Antonio Bergnoli⁶⁰ Daniel Bick⁴⁹ Lukas Bieger⁵⁴ Svetlana Biktemerova⁶⁷ Thilo Birkenfeld⁴⁸ Iwan Blake³¹ Simon Blyth¹⁰ Anastasia Bolshakova⁶⁷ Mathieu Bongrand⁴⁷ Dominique Breton⁴³ Augusto Brigatti⁵⁷ Riccardo Brugnera⁶¹ Riccardo Bruno⁵⁵ Antonio Budano⁶⁴ Jose Busto⁴⁶ Anatael Cabrera⁴³ Barbara Caccianiga⁵⁷ Hao Cai³⁴ Xiao Cai¹⁰ Yanke Cai¹⁰ Zhiyan Cai¹⁰ Stéphane Callier⁴⁴ Steven Calvez⁴⁷ Antonio Cammi⁵⁹ Agustin Campeny^{6,5} Chuanya Cao¹⁰ Guofu Cao¹⁰ Jun Cao¹⁰ Rossella Caruso⁵⁵ Cédric Cerna⁴⁴ Vanessa Cerrone⁶¹ Jinfan Chang¹⁰ Yun Chang³⁹ Auttakit Chatrabhuti⁷¹ Chao Chen¹⁰ Guoming Chen²⁸ Pingping Chen¹⁹ Shaomin Chen¹³ Xin Chen^{27,10} Yiming Chen¹⁰ Yixue Chen¹¹ Yu Chen²¹ Zelin Chen^{27,10} Zhangming Chen³⁰ Zhiyuan Chen¹⁰ Zikang Chen²¹ Jie Cheng¹¹ Yaping Cheng⁷ Yu Chin Cheng⁴⁰ Alexander Chepurnov⁶⁹ Alexey Chetverikov⁶⁷ Davide Chiesa⁵⁸ Pietro Chimenti³ Yen-Ting Chin⁴⁰ Po-Lin Chou³⁸ Ziliang Chu¹⁰ Artem Chukanov⁶⁷ Gérard Claverie⁴⁴ Catia Clementi⁶² Barbara Clerbaux² Marta Colomer Molla² Selma Conforti Di Lorenzo⁴⁴ Alberto Coppi⁶¹ Daniele Corti⁶⁰ Simon Csakli⁵² Chenyang Cui¹⁰ Flavio Dal Corso⁶⁰ Olivia Dalager⁷⁵ Jaydeep Datta² Christophe De La Taille⁴⁴ Zhi Deng¹³ Ziyang Deng¹⁰ Xiaoyu Ding²⁶ Xuefeng Ding¹⁰ Yayun Ding¹⁰ Bayu Dirgantara⁷³ Carsten Dittrich⁵² Sergey Dmitrievsky⁶⁷ Tadeas Dohnal⁴¹ Dmitry Dolzhikov⁶⁷ Georgy Donchenko⁶⁹ Jianmeng Dong¹³ Evgeny Doroshkevich⁶⁸ Wei Dou¹³ Marcos Dracos⁴⁵ Frédéric Druillolle⁴⁴ Ran Du¹⁰ Shuxian Du³⁷ Yujie Duan³⁴ Katherine Dugas⁷⁵ Stefano Dusini⁶⁰ Hongyue Duyang²⁶ Jessica Eck⁵⁴ Timo Enqvist⁴² Andrea Fabbri⁶⁴ Ulrike Fahrenholz⁵² Lei Fan¹⁰ Jian Fang¹⁰ Wenxing Fang¹⁰ Dmitry Fedoseev⁶⁷ Li-Cheng Feng³⁸ Qichun Feng²² Federico Ferraro⁵⁷ Amélie Fournier⁴⁴ Fritsch Fritsch⁴⁵ Haonan Gan³² Feng Gao⁴⁸ Feng Gao² Alberto Garfagnini⁶¹ Arsenii Gavrikov⁶¹ Marco Giammarchi⁵⁷ Nunzio Giudice⁵⁵ Maxim Gonchar⁶⁷ Guanghua Gong¹³ Hui Gong¹³ Yuri Gornushkin⁶⁷ Marco Grassi⁶¹ Maxim Gromov⁶⁹ Vasily Gromov⁶⁷ Minghao Gu¹⁰ Xiaofei Gu³⁷ Yu Gu²⁰ Mengyun Guan¹⁰ Yuduo Guan¹⁰ Nunzio Guardone⁵⁵ Rosa Maria Guizzetti⁶¹ Cong Guo¹⁰ Wanlei Guo¹⁰ Caren Hagner⁴⁹ Hechong Han¹⁰ Ran Han⁷ Yang Han²¹ Jinhong He³⁴ Miao He¹⁰ Wei He¹⁰ Xinhai He¹⁰ Tobias Heinz⁵⁴ Patrick Hellmuth⁴⁴ Yuekun

Heng¹⁰ Rafael Herrera^{6,5} YuenKeung Hor²¹ Shaojing Hou¹⁰ Yee Hsiung⁴⁰ Bei-Zhen Hu⁴⁰ Hang Hu²¹ Jun Hu¹⁰ Peng Hu¹⁰ Shouyang Hu⁹ Tao Hu¹⁰ Yuxiang Hu^{10,14} Zhuojun Hu²¹ Guihong Huang²⁵ Hanxiong Huang⁹ Jinhao Huang¹⁰ Junting Huang³⁰ Kaixuan Huang²¹ Shengheng Huang²⁵ Wenhao Huang²⁶ Xin Huang¹⁰ Xingtiao Huang²⁶ Yongbo Huang²⁸ Jiaqi Hui³⁰ Lei Huo²² Wenju Huo²³ Cédric Huss⁴⁴ Safeer Hussain⁶⁶ Leonard Imbert⁴⁷ Ara Ioannisian¹ Roberto Isocrate⁶⁰ Arshak Jafar⁵¹ Beatrice Jelmini⁶¹ Ignacio Jeria⁶ Xiaolu Ji¹⁰ Huihui Jia³³ Junji Jia³⁴ Siyu Jian⁹ Cailian Jiang²⁷ Di Jiang²³ Guangzheng Jiang¹⁷ Wei Jiang¹⁰ Xiaoshan Jiang¹⁰ Xiaozhao Jiang¹⁰ Yixuan Jiang¹⁰ Xiaoping Jing¹⁰ Cécile Jollet⁴⁴ Li Kang¹⁹ Rebin Karaparabil⁴⁵ Narine Kazarian¹ Ali Khan⁶⁶ Amina Khatun⁷⁰ Khanchai Khosonthongkee⁷³ Denis Korablev⁶⁷ Konstantin Kouzakov⁶⁹ Alexey Krasnoperov⁶⁷ Sergey Kuleshov⁵ Sindhujha Kumaran⁷⁵ Nikolay Kutovskiy⁶⁷ Loïc Labit⁴⁴ Tobias Lachenmaier⁵⁴ Haojing Lai³⁰ Cecilia Landini⁵⁷ Sébastien Leblanc⁴⁴ Frederic Lefevre⁴⁷ Ruiting Lei¹⁹ Rupert Leitner⁴¹ Jason Leung³⁸ Demin Li³⁷ Fei Li¹⁰ Fule Li¹³ Gaosong Li¹⁰ Hongjian Li¹⁰ Huang Li¹⁰ Jiajun Li²¹ Min Li¹⁰ Nan Li¹⁶ Qingjiang Li¹⁶ Ruhui Li¹⁰ Rui Li³⁰ Shanfeng Li¹⁹ Shuo Li²⁷ Tao Li²¹ Teng Li²⁶ Weidong Li^{10,14} Weiguo Li¹⁰ Xiaomei Li⁹ Xiaonan Li¹⁰ Xinglong Li⁹ Yi Li¹⁹ Yichen Li¹⁰ Yufeng Li¹⁰ Zhaohan Li¹⁰ Zhibing Li²¹ Ziyuan Li²¹ Zonghai Li³⁴ An-An Liang³⁸ Hao Liang⁹ Hao Liang²³ Jiajun Liao²¹ Yilin Liao³⁰ Yuzhong Liao³² Ayut Limphirat⁷³ Guey-Lin Lin³⁸ Shengxin Lin¹⁹ Tao Lin¹⁰ Jiajie Ling²¹ Xin Ling²⁴ Ivano Lippi⁶⁰ Caimei Liu¹⁰ Fang Liu¹¹ Fengcheng Liu¹¹ Haidong Liu³⁷ Haotian Liu³⁴ Hongbang Liu²⁸ Hongjuan Liu²⁴ Hongtao Liu²¹ Hongyang Liu¹⁰ Jianglai Liu^{30,31} Jiayi Liu¹⁰ Jinchang Liu¹⁰ Min Liu²⁴ Qian Liu¹⁴ Qin Liu²³ Runxuan Liu^{53,50,48} Shenghui Liu¹⁰ Shubin Liu²³ Shulin Liu¹⁰ Xiaowei Liu²¹ Xiwen Liu²⁸ Xuewei Liu¹³ Yankai Liu³⁵ Zhen Liu¹⁰ Lorenzo Loi⁵⁸ Alexey Lokhov^{69,68} Paolo Lombardi⁵⁷ Claudio Lombardo⁵⁵ Kai Loo⁴² Chuan Lu³² Haoqi Lu¹⁰ Jingbin Lu¹⁵ Junguang Lu¹⁰ Meishu Lu⁵² Peizhi Lu²¹ Shuxiang Lu³⁷ Xianguo Lu⁷⁴ Bayarto Lubsandorzhev⁶⁸ Sultim Lubsandorzhev⁶⁸ Livia Ludhova^{50,48} Arslan Lukanov⁶⁸ Fengjiao Luo²⁴ Guang Luo²¹ Jianyi Luo²¹ Shu Luo³⁶ Wuming Luo¹⁰ Xiaojie Luo¹⁰ Vladimir Lyashuk⁶⁸ Bangzheng Ma²⁶ Bing Ma³⁷ Qiumei Ma¹⁰ Si Ma¹⁰ Xiaoyan Ma¹⁰ Xubo Ma¹¹ Jihane Maalmi⁴³ Jingyu Mai²¹ Marco Malabarba^{53,50} Yury Malyskin^{53,50} Roberto Carlos Mandujano⁷⁵ Fabio Mantovani⁵⁶ Xin Mao⁷ Yajun Mao¹² Stefano M. Mari⁶⁴ Filippo Marini⁶¹ Agnese Martini⁶³ Matthias Mayer⁵² Davit Mayilyan¹ Ints Mednieks⁶⁵ Yue Meng³⁰ Anita Meraviglia^{53,50,48} Anselmo Mereaglia⁴⁴ Emanuela Meroni⁵⁷ Lino Miramonti⁵⁷ Nikhil Mohan^{53,50,48} Michele Montuschi⁵⁶ Cristobal Morales Reveno^{53,50,48} Massimiliano Nastasi⁵⁸ Dmitry V. Naumov⁶⁷ Elena Naumova⁶⁷ Diana Navas-Nicolas⁴³ Igor Nemchenok⁶⁷ Minh Thuan Nguyen Thi³⁸ Alexey Nikolaev⁶⁹ Feipeng Ning¹⁰ Zhe Ning¹⁰ Hiroshi Nunokawa⁴ Lothar Oberauer⁵² Juan Pedro Ochoa-Ricoux^{75,6,5} Alexander Olshevskiy⁶⁷ Domizia Orestano⁶⁴ Fausto Ortica⁶² Rainer Othegraven⁵¹ Alessandro Paoloni⁶³ George Parker⁵¹ Sergio Parmeggiano⁵⁷ Achilleas Patsias⁴⁸ Yatian Pei¹⁰ Luca Pelicci^{50,48} Anguo Peng²⁴ Haiping Peng²³ Yu Peng¹⁰ Zhaoyuan Peng¹⁰ Elisa Percalli⁵⁷ Willy Perrin⁴⁵ Frédéric Perrot⁴⁴ Pierre-Alexandre Petitjean² Fabrizio Petrucci⁶⁴ Oliver Pilarczyk⁵¹ Luis Felipe Piñeres Rico⁴⁵ Artyom Popov⁶⁹ Pascal Poussot⁴⁵ Ezio Previtali⁵⁸ Fazhi Qi¹⁰ Ming Qi²⁷ Xiaohui Qi¹⁰ Sen

Qian¹⁰ Xiaohui Qian¹⁰ Zhen Qian²¹ Hao Qiao¹² Zhonghua Qin¹⁰ Shoukang Qiu²⁴
 Manhao Qu³⁷ Zhenning Qu¹⁰ Gioacchino Ranucci⁵⁷ Alessandra Re⁵⁷ Abdel Rebi⁴⁴
 Mariia Redchuk⁶⁰ Gioele Reina⁵⁷ Bin Ren¹⁹ Jie Ren⁹ Yuhang Ren¹⁰ Barbara Ricci⁵⁶
 Komkrit Rientong⁷¹ Mariam Rifai^{50,48} Mathieu Roche⁴⁴ Narongkiat Rodphai¹⁰ Aldo
 Romani⁶² Bedřich Roskovec⁴¹ Xichao Ruan⁹ Arseniy Rybnikov⁶⁷ Andrey Sadovsky⁶⁷
 Paolo Saggese⁵⁷ Deshan Sandanayake⁴⁵ Anut Sangka⁷² Giuseppe Sava⁵⁵ Utane
 Sawangwit⁷² Michaela Schever^{50,48} Cédric Schwab⁴⁵ Konstantin Schweizer⁵² Alexandr
 Selyunin⁶⁷ Andrea Serafini⁶¹ Mariangela Settimo⁴⁷ Junyu Shao¹⁰ Vladislav Sharov⁶⁷
 Hexi Shi^{53,50} Jingyan Shi¹⁰ Yanan Shi¹⁰ Vitaly Shutov⁶⁷ Andrey Sidorenkov⁶⁸ Fedor
 Šimkovic⁷⁰ Apeksha Singhal^{50,48} Chiara Sirignano⁶¹ Jaruchit Siripak⁷³ Monica Sisti⁵⁸
 Mikhail Smirnov²¹ Oleg Smirnov⁶⁷ Sergey Sokolov⁶⁷ Julanan Songwadhana⁷³
 Boonrucksar Soonthornthum⁷² Albert Sotnikov⁶⁷ Warintorn Sreethawong⁷³ Achim
 Stahl⁴⁸ Luca Stanco⁶⁰ Konstantin Stankevich⁶⁹ Hans Steiger^{52,51} Jochen Steinmann⁴⁸
 Tobias Sterr⁵⁴ Matthias Raphael Stock⁵² Virginia Strati⁵⁶ Michail Strizh⁶⁹ Alexander
 Studenikin⁶⁹ Aoqi Su³⁷ Jun Su⁸ Jun Su²¹ Guangbao Sun³⁴ Shifeng Sun¹¹ Xilei Sun¹⁰
 Yongjie Sun²³ Yongzhao Sun¹⁰ Zhengyang Sun³¹ Narumon Suwonjandee⁷¹ Akira
 Takenaka³¹ Xiaohan Tan²⁶ Jian Tang²¹ Jingzhe Tang²⁸ Qiang Tang²¹ Quan Tang²⁴
 Xiao Tang¹⁰ Vidhya Thara Hariharan⁴⁹ Igor Tkachev⁶⁸ Tomas Tmej⁴¹ Marco Danilo
 Claudio Torri⁵⁷ Andrea Triossi⁶¹ Wladyslaw Trzaska⁴² Yu-Chen Tung⁴⁰ Cristina Tuve⁵⁵
 Nikita Ushakov⁶⁸ Vadim Vedin⁶⁵ Carlo Venettacci⁶⁴ Giuseppe Verde⁵⁵ Maxim
 Vialkov⁶⁹ Benoit Viaud⁴⁷ Cornelius Moritz Vollbrecht^{53,50,48} Katharina von Sturm⁶¹
 Vit Vorobel⁴¹ Dmitriy Voronin⁶⁸ Lucia Votano⁶³ Pablo Walker^{6,5} Caishen Wang¹⁹
 Chung-Hsiang Wang³⁹ En Wang³⁷ Guoli Wang²² Hanwen Wang¹⁰ Jian Wang²³ Jun
 Wang²¹ Li Wang^{37,10} Lu Wang¹⁰ Meng Wang²⁴ Meng Wang²⁶ Mingyuan Wang¹⁰
 Qianchuan Wang³⁴ Ruiguang Wang¹⁰ Sibao Wang¹⁰ Siguang Wang¹² Wei Wang²¹
 Wenshuai Wang¹⁰ Xi Wang¹⁶ Xiangyue Wang²¹ Yangfu Wang¹⁰ Yaoguang Wang²⁶ Yi
 Wang¹⁰ Yi Wang¹³ Yifang Wang¹⁰ Yuanqing Wang¹³ Yuyi Wang¹³ Zhe Wang¹³
 Zheng Wang¹⁰ Zhimin Wang¹⁰ Apimook Watcharangkul⁷² Wei Wei¹⁰ Wei Wei²⁶
 Wenlu Wei¹⁰ Yadong Wei¹⁹ Yuehuan Wei²¹ Liangjian Wen¹⁰ Jun Weng¹³ Christopher
 Wiebusch⁴⁸ Rosmarie Wirth⁴⁹ Chengxin Wu²¹ Diru Wu¹⁰ Qun Wu²⁶ Yinhui Wu¹⁰
 Yiyang Wu¹³ Zhi Wu¹⁰ Michael Wurm⁵¹ Jacques Wurtz⁴⁵ Christian Wysotzki⁴⁸ Yufei
 Xi³² Dongmei Xia¹⁸ Shishen Xian³¹ Ziqian Xiang³⁰ Fei Xiao¹⁰ Xiang Xiao²¹ Xiaochuan
 Xie²⁸ Yijun Xie¹⁰ Yuguang Xie¹⁰ Zhao Xin¹⁰ Zhizhong Xing¹⁰ Benda Xu¹³ Cheng Xu²⁴
 Donglian Xu^{31,30} Fanrong Xu²⁰ Hangkun Xu¹⁰ Jiayang Xu¹⁰ Jilei Xu¹⁰ Jing Xu⁸
 Jinghuan Xu²⁸ Meihang Xu¹⁰ Xunjie Xu¹⁰ Yin Xu³³ Yu Xu²¹ Baojun Yan¹⁰ Qiyu
 Yan^{14,74} Taylor Yan⁷³ Xiongbo Yan¹⁰ Yupeng Yan⁷³ Changgen Yang¹⁰ Chengfeng
 Yang²¹ Fengfan Yang¹⁰ Jie Yang³⁷ Lei Yang¹⁹ Pengfei Yang²¹ Xiaoyu Yang¹⁰ Yifan
 Yang² Yixiang Yang¹⁰ Zekun Yang²⁶ Haifeng Yao¹⁰ Jiaxuan Ye¹⁰ Mei Ye¹⁰ Ziping
 Ye³¹ Frédéric Yermia⁴⁷ Zhengyun You²¹ Boxiang Yu¹⁰ Chiye Yu¹⁹ Chunxu Yu³³
 Guojun Yu²⁷ Hongzhao Yu²¹ Miao Yu³⁴ Xianghui Yu³³ Zeyuan Yu¹⁰ Zezhong Yu¹⁰
 Cenxi Yuan²¹ Chengzhuo Yuan¹⁰ Ying Yuan¹² Zhenxiong Yuan¹³ Baobiao Yue²¹
 Noman Zafar⁶⁶ Kirill Zamogilnyi⁶⁹ Vitalii Zavadskyi⁶⁷ Fanrui Zeng²⁶ Shan Zeng¹⁰
 Tingxuan Zeng¹⁰ Yuda Zeng²¹ Liang Zhan¹⁰ Aiqiang Zhang¹³ Bin Zhang³⁷ Binting

Zhang¹⁰ Feiyang Zhang³⁰ Hangchang Zhang¹⁰ Haosen Zhang¹⁰ Honghao Zhang²¹
 Jialiang Zhang²⁷ Jiawen Zhang¹⁰ Jie Zhang¹⁰ Jingbo Zhang²² Jinnan Zhang¹⁰ Junwei
 Zhang²⁸ Lei Zhang²⁷ Peng Zhang¹⁰ Ping Zhang³⁰ Qingmin Zhang³⁵ Shiqi Zhang²¹
 Shu Zhang²¹ Shuihan Zhang¹⁰ Siyuan Zhang²⁸ Tao Zhang³⁰ Xiaomei Zhang¹⁰ Xin
 Zhang¹⁰ Xuanton Zhang¹⁰ Yibing Zhang¹⁰ Yinhong Zhang¹⁰ Yiyu Zhang¹⁰ Yongpeng
 Zhang¹⁰ Yu Zhang¹⁰ Yuanyuan Zhang³¹ Yumei Zhang²¹ Zhenyu Zhang³⁴ Zhijian
 Zhang¹⁹ Jie Zhao¹⁰ Rong Zhao²¹ Runze Zhao¹⁰ Shujun Zhao³⁷ Tianhao Zhao¹⁰ Hua
 Zheng¹⁹ Yangheng Zheng¹⁴ Jing Zhou⁹ Li Zhou¹⁰ Nan Zhou²³ Shun Zhou¹⁰ Tong
 Zhou¹⁰ Xiang Zhou³⁴ Xing Zhou¹⁰ Jingsen Zhu^{21,29} Kangfu Zhu³⁵ Kejun Zhu¹⁰
 Zhihang Zhu¹⁰ Bo Zhuang¹⁰ Honglin Zhuang¹⁰ Liang Zong¹³ Jiaheng Zou¹⁰

¹ Yerevan Physics Institute, Yerevan, Armenia

² Université Libre de Bruxelles, Brussels, Belgium

³ Universidade Estadual de Londrina, Londrina, Brazil

⁴ Pontificia Universidade Catolica do Rio de Janeiro, Rio de Janeiro, Brazil

⁵ Millennium Institute for SubAtomic Physics at the High-energy Frontier (SAPHIR), ANID, Chile

⁶ Pontificia Universidad Católica de Chile, Santiago, Chile

⁷ Beijing Institute of Spacecraft Environment Engineering, Beijing, China

⁸ Beijing Normal University, Beijing, China

⁹ China Institute of Atomic Energy, Beijing, China

¹⁰ Institute of High Energy Physics, Beijing, China

¹¹ North China Electric Power University, Beijing, China

¹² School of Physics, Peking University, Beijing, China

¹³ Tsinghua University, Beijing, China

¹⁴ University of Chinese Academy of Sciences, Beijing, China

¹⁵ Jilin University, Changchun, China

¹⁶ College of Electronic Science and Engineering, National University of Defense Technology, Changsha, China

¹⁷ Chengdu University of Technology, Chengdu, China

¹⁸ Chongqing University, Chongqing, China

¹⁹ Dongguan University of Technology, Dongguan, China

²⁰ Jinan University, Guangzhou, China

²¹ Sun Yat-Sen University, Guangzhou, China

²² Harbin Institute of Technology, Harbin, China

²³ University of Science and Technology of China, Hefei, China

²⁴ The Radiochemistry and Nuclear Chemistry Group in University of South China, Hengyang, China

²⁵ Wuyi University, Jiangmen, China

²⁶ Shandong University, Jinan, China, and Key Laboratory of Particle Physics and Particle Irradiation of Ministry of Education, Shandong University, Qingdao, China

²⁷ Nanjing University, Nanjing, China

²⁸ Guangxi University, Nanning, China

²⁹ East China University of Science and Technology, Shanghai, China

³⁰ School of Physics and Astronomy, Shanghai Jiao Tong University, Shanghai, China

³¹ Tsung-Dao Lee Institute, Shanghai Jiao Tong University, Shanghai, China

- ³²*Institute of Hydrogeology and Environmental Geology, Chinese Academy of Geological Sciences, Shijiazhuang, China*
- ³³*Nankai University, Tianjin, China*
- ³⁴*Wuhan University, Wuhan, China*
- ³⁵*Xi'an Jiaotong University, Xi'an, China*
- ³⁶*Xiamen University, Xiamen, China*
- ³⁷*School of Physics and Microelectronics, Zhengzhou University, Zhengzhou, China*
- ³⁸*Institute of Physics, National Yang Ming Chiao Tung University, Hsinchu*
- ³⁹*National United University, Miao-Li*
- ⁴⁰*Department of Physics, National Taiwan University, Taipei*
- ⁴¹*Charles University, Faculty of Mathematics and Physics, Prague, Czech Republic*
- ⁴²*University of Jyväskylä, Department of Physics, Jyväskylä, Finland*
- ⁴³*IJCLab, Université Paris-Saclay, CNRS/IN2P3, 91405 Orsay, France*
- ⁴⁴*Univ. Bordeaux, CNRS, LP2I, UMR 5797, F-33170 Gradignan,, F-33170 Gradignan, France*
- ⁴⁵*IPHC, Université de Strasbourg, CNRS/IN2P3, F-67037 Strasbourg, France*
- ⁴⁶*Aix Marseille Univ, CNRS/IN2P3, CPPM, Marseille, France*
- ⁴⁷*SUBATECH, Université de Nantes, IMT Atlantique, CNRS-IN2P3, Nantes, France*
- ⁴⁸*III. Physikalisches Institut B, RWTH Aachen University, Aachen, Germany*
- ⁴⁹*Institute of Experimental Physics, University of Hamburg, Hamburg, Germany*
- ⁵⁰*Forschungszentrum Jülich GmbH, Nuclear Physics Institute IKP-2, Jülich, Germany*
- ⁵¹*Institute of Physics and EC PRISMA⁺, Johannes Gutenberg Universität Mainz, Mainz, Germany*
- ⁵²*Technische Universität München, München, Germany*
- ⁵³*Helmholtzzentrum für Schwerionenforschung, Planckstrasse 1, D-64291 Darmstadt, Germany*
- ⁵⁴*Eberhard Karls Universität Tübingen, Physikalisches Institut, Tübingen, Germany*
- ⁵⁵*INFN Catania and Dipartimento di Fisica e Astronomia dell'Università di Catania, Catania, Italy*
- ⁵⁶*Department of Physics and Earth Science, University of Ferrara and INFN Sezione di Ferrara, Ferrara, Italy*
- ⁵⁷*INFN Sezione di Milano and Dipartimento di Fisica dell'Università di Milano, Milano, Italy*
- ⁵⁸*INFN Milano Bicocca and University of Milano Bicocca, Milano, Italy*
- ⁵⁹*INFN Milano Bicocca and Politecnico of Milano, Milano, Italy*
- ⁶⁰*INFN Sezione di Padova, Padova, Italy*
- ⁶¹*Dipartimento di Fisica e Astronomia dell'Università di Padova and INFN Sezione di Padova, Padova, Italy*
- ⁶²*INFN Sezione di Perugia and Dipartimento di Chimica, Biologia e Biotecnologie dell'Università di Perugia, Perugia, Italy*
- ⁶³*Laboratori Nazionali di Frascati dell'INFN, Roma, Italy*
- ⁶⁴*University of Roma Tre and INFN Sezione Roma Tre, Roma, Italy*
- ⁶⁵*Institute of Electronics and Computer Science, Riga, Latvia*
- ⁶⁶*Pakistan Institute of Nuclear Science and Technology, Islamabad, Pakistan*
- ⁶⁷*Joint Institute for Nuclear Research, Dubna, Russia*
- ⁶⁸*Institute for Nuclear Research of the Russian Academy of Sciences, Moscow, Russia*
- ⁶⁹*Lomonosov Moscow State University, Moscow, Russia*

⁷⁰*Comenius University Bratislava, Faculty of Mathematics, Physics and Informatics, Bratislava, Slovakia*

⁷¹*High Energy Physics Research Unit, Department of Physics, Faculty of Science, Chulalongkorn University, Bangkok, Thailand*

⁷²*National Astronomical Research Institute of Thailand, Chiang Mai, Thailand*

⁷³*Suranaree University of Technology, Nakhon Ratchasima, Thailand*

⁷⁴*University of Warwick, University of Warwick, Coventry, CV4 7AL, United Kingdom*

⁷⁵*Department of Physics and Astronomy, University of California, Irvine, California, USA*

E-mail: Juno_pub_comm@juno.ihep.ac.cn

ABSTRACT: We explore the decay of bound neutrons into invisible particles (e.g., $n \rightarrow 3\nu$ or $nn \rightarrow 2\nu$) in the JUNO liquid scintillator detector, which do not produce an observable signal. The invisible decay includes two decay modes: $n \rightarrow inv$ and $nn \rightarrow inv$. The invisible decays of s -shell neutrons in ^{12}C will leave a highly excited residual nucleus. Subsequently, some de-excitation modes of the excited residual nuclei can produce a time- and space-correlated triple coincidence signal in the JUNO detector. Based on a full Monte Carlo simulation informed with the latest available data, we estimate all backgrounds, including inverse beta decay events of the reactor antineutrino $\bar{\nu}_e$, natural radioactivity, cosmogenic isotopes and neutral current interactions of atmospheric neutrinos. Pulse shape discrimination and multivariate analysis techniques are employed to further suppress backgrounds. With two years of exposure, JUNO is expected to give an order of magnitude improvement compared to the current best limits. After 10 years of data taking, the JUNO expected sensitivities at a 90% confidence level are $\tau/B(n \rightarrow inv) > 5.0 \times 10^{31}$ yr and $\tau/B(nn \rightarrow inv) > 1.4 \times 10^{32}$ yr.

Contents

1	Introduction	1
2	JUNO detector	2
3	Simulation	3
3.1	Neutron invisible decays	3
3.2	Background sources	5
4	Event selection	8
4.1	Muon veto strategy	9
4.2	Event selection	10
5	Background estimation	12
5.1	$n \rightarrow inv$ analysis	13
5.2	$nn \rightarrow inv$ analysis	16
6	Sensitivity	19
7	Conclusion	21

1 Introduction

The conservation of the baryon number B is an accidental symmetry in the Standard Model of particle physics, and no fundamental symmetry guarantees the proton’s stability. Baryon number violation is one of three basic ingredients to generate the cosmological matter-antimatter asymmetry from an initially symmetrical universe [1]. On the other hand, baryon number B is necessarily violated, and the proton must decay in the Grand Unified Theories (GUTs) [2], which can unify the strong, weak, and electromagnetic interactions into a single underlying force. These GUTs have motivated a long history of experiments searching for proton decay [3]. However, no experimental evidence to date for proton decay or B -violating neutron decay has been found [4]. Discovering nucleon decay now remains a key signature of GUTs. Super-Kamiokande with Gd-loaded water can improve its background rejection capability in the nucleon decay searches [5]. The new generation of underground experiments such as JUNO [6–8], Hyper-Kamiokande [9] and DUNE [10] with tens or even hundreds of kiloton target masses and different detection technologies, will continue to search for the nucleon decay and test GUTs.

JUNO is a 20 kton multipurpose underground liquid scintillator (LS) detector under construction in China, with a 650-meter rock overburden (1800 m.w.e.) for shielding against cosmic rays [6–8]. The LS detectors have distinct advantages in the search for some nucleon

decay modes, such as $p \rightarrow \bar{\nu}K^+$ [11–13] and the neutron invisible decays [14, 15]. The proton decay mode $p \rightarrow \bar{\nu}K^+$ is one of the two dominant decay modes predicted by a majority of GUTs [16]. The JUNO expected sensitivity will reach $\tau/B(p \rightarrow \bar{\nu}K^+) > 9.6 \times 10^{33}$ yr with 10 years of data taking [13], which is higher than the current best limit of 5.9×10^{33} yr from the Super-Kamiokande experiment [17]. The neutron invisible decay has two modes: $n \rightarrow inv$ and $nn \rightarrow inv$. Invisible modes are dominant in some new physics models [18–21]. The SNO+ experiment sets the current best limit for single neutron disappearance at $\tau/B(n \rightarrow inv) > 9.0 \times 10^{29}$ years (90% C.L.), while for the $nn \rightarrow inv$ mode, the best limit is provided by the KamLAND experiment with $\tau/B(nn \rightarrow inv) > 1.4 \times 10^{30}$ years (90% C.L.) [14, 15, 22].

In this paper, the JUNO potential for neutron invisible decays is investigated. Sec. 2 briefly introduces the JUNO detector and its expected performance. In Sec. 3, we describe the Monte Carlo (MC) simulation of neutron invisible decays and all background sources. In Sec. 4, some basic event selection criteria are developed to discriminate the neutron invisible decays from the backgrounds. In Sec. 5, we estimate all possible backgrounds in detail and use the pulse shape discrimination and multivariate analysis techniques to further suppress them. Sec. 6 presents the expected JUNO sensitivities to the neutron invisible decays. Finally, a conclusion is given in Sec. 7.

2 JUNO detector

As a multipurpose neutrino observatory, JUNO comprises a central detector (CD), veto detector, and calibration system [7, 8] as shown in Fig. 1. The CD holds 20 kton of LS [23] filled in an acrylic shell with an inner diameter of 35.4 m, which is immersed in a cylindrical water pool (WP) with both diameter and height of 43.5 m. There are 17,612 high quantum efficiency 20-inch PMTs (LPMTs) and 25,600 3-inch PMTs (SPMTs), yielding an integral 77.9% photo-cathode coverage, closely packed around the LS ball, aiming to achieve an energy resolution of $\leq 3\%$ at 1 MeV. Two kinds of LPMTs, MCP-PMT from NNVT and dynode PMT from Hamamatsu, are used [24]. The veto detector, optically decoupled from the CD, is designed to tag cosmic muons with high efficiency and to precisely track performance for the purpose of background reduction. The veto system includes a water Cherenkov detector (WCD) and a top tracker (TT) surrounding the CD to shield the neutrons and the natural radioactivity from the rock. The water Cherenkov detector is made of 35 kton of ultrapure water with a radon concentration below 0.2 Bq/m^3 [7], which is supplied and maintained by a circulation system. The Cherenkov light is detected by 2400 20-inch PMTs, and its muon detection efficiency is expected to reach 99.5% [7]. The top tracker is made of reused plastic scintillators from the OPERA experiment, and it covers half of the water pool on top with a 3-layer configuration for the muon track angular reconstruction precision of 0.20° [25]. The calibration system includes the deployment of sources along the central axis from an automated calibration unit (ACU). It also consists of a cable loop system which allows for position these sources to off-axis positions on a plane. Additionally, there is a remotely operated vehicle and a guide tube system outside of the acrylic sphere to study boundary effects [26, 27].

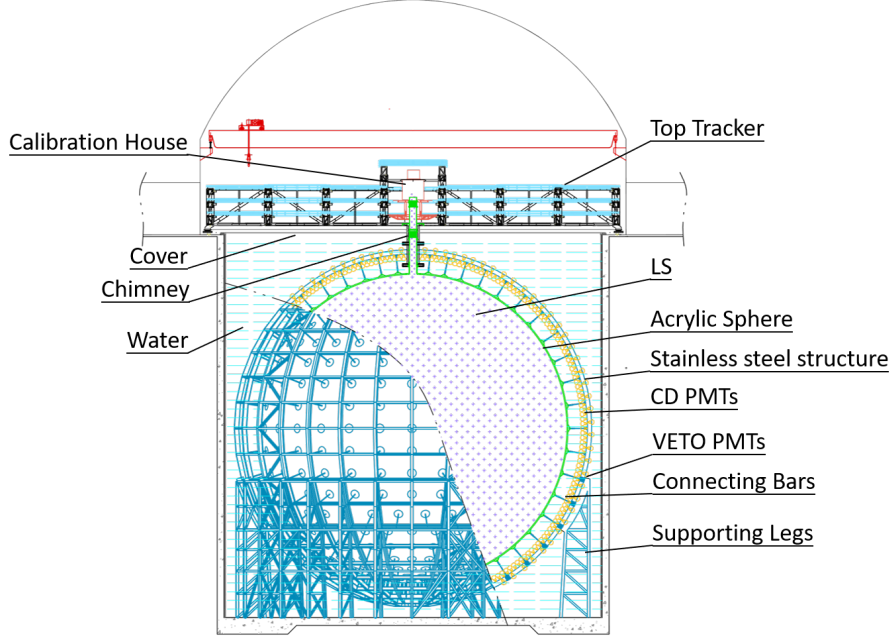


Figure 1. Schematic of the JUNO detector.

3 Simulation

To understand the detector signature of neutron invisible decays and discriminate them from the backgrounds in the JUNO detector, a full MC simulation has been performed with the JUNO simulation framework [28]. The simulation accounts for the response of the detector and electronics, as well as the performance of the energy and vertex reconstructions. The detector simulation employs GEANT4 [29]. The electronics simulation [30] incorporates factors such as dark noise, transit time spread, and afterpulses. To build the hit time and charge information of each readout signal, we adopt the deconvolution method in the step of waveform reconstruction [31]. Furthermore, the maximum likelihood estimation strategy from Ref. [32], combining charge and time, is used for energy and vertex reconstruction. All background sources are described and simulated in this section, including the inverse beta decay (IBD) events from the reactor antineutrino $\bar{\nu}_e$, natural radioactivity, cosmogenic isotopes and fast neutrons from the cosmic-ray muons, and atmospheric neutrino events.

3.1 Neutron invisible decays

The JUNO LS includes about 88% ^{12}C and 12% ^1H [6]. The invisible decays of neutrons from the s -shell in ^{12}C will lead to a highly excited residual nucleus. Then the excited nucleus can emit secondary particles (p, n, α, γ) and leave a daughter nucleus. In Ref. [14], Kamyshev and Kolbe have analyzed one and two neutron invisible decays from ^{12}C based on the statistical model code SMOKER [33]. It has been found that some de-excitation modes of the excited nucleus can give time-, energy-, and space-correlated signals in the

LS detector. Here we consider the following four de-excitation modes [14, 33]:

$$^{11}\text{C}^* \rightarrow n + ^{10}\text{C} \quad (B_{n1} = 3.0\%), \quad (3.1)$$

$$^{11}\text{C}^* \rightarrow n + \gamma + ^{10}\text{C} \quad (B_{n2} = 2.8\%), \quad (3.2)$$

$$^{10}\text{C}^* \rightarrow n + ^9\text{C} \quad (B_{nn1} = 6.2\%), \quad (3.3)$$

$$^{10}\text{C}^* \rightarrow n + p + ^8\text{B} \quad (B_{nn2} = 6.0\%), \quad (3.4)$$

where the daughter nuclei $^{10}\text{C}(\beta^+, 19.3 \text{ s}, 3.65 \text{ MeV})$, $^9\text{C}(\beta^+, 0.127 \text{ s}, 16.5 \text{ MeV})$, and $^8\text{B}(\beta^+\alpha, 0.770 \text{ s}, 18.0 \text{ MeV})$ are radioactive. The corresponding decay mode, half-life, and energy release have been indicated in parentheses. The de-excitation modes in Eqs. (3.1) and (3.2) for the single neutron invisible decay $n \rightarrow inv$ have branching ratios of $B_{n1} = 3.0\%$ and $B_{n2} = 2.8\%$, respectively. For the two neutron invisible decays $nn \rightarrow inv$, the de-excitation modes in Eqs. (3.3) and (3.4) exhibit the branching ratios of $B_{nn1} = 6.2\%$ and $B_{nn2} = 6.0\%$.

Note that the above four de-excitation modes feature a triple coincidence signal in the LS detector [14]. The first signal comes from neutron elastic and inelastic scatterings with free protons and ^{12}C . The de-excitation products γ and p can also contribute to this first signal of the triple coincidence event. The neutron will quickly slow down and be thermalized after many collisions. In the LS, these thermalized neutrons are captured by a free proton $\sim 220 \mu\text{s}$ later and give a second signal of the 2.2 MeV γ ray. The third signal arises from the β^+ decay of the daughter nuclei ^{10}C , ^9C , and ^8B . The strong time-, energy-, and space-correlation between the three signals can be exploited to significantly suppress backgrounds.

We have made an event generator and used it to generate 0.5 million events for each de-excitation mode in Eqs. (3.1)-(3.4). Here, the neutron kinetic energy distributions in Figs. 4 and 6 of Ref. [14] have been used. The emitted γ in Eq. (3.2) is dominated by a strong monoenergetic line at 3.35 MeV, which is produced from the decay of the first excited 2^+ state of ^{10}C [14]. The ejected proton from Eq. (3.4) is monoenergetic with an energy of 0.922 MeV, which corresponds to the de-excitation of the first excited state of ^9C [14]. The kinetic energies of the daughter nuclei ^{10}C , ^9C , and ^8B have been set to zero. Then we simulate these events from $n \rightarrow inv$ and $nn \rightarrow inv$ and obtain the energy, spatial, and time interval distributions of these triple coincidence signals. In this work, E_i (R_i) is used to denote the reconstructed energy (radial position) of the i^{th} signal with $i = 1, 2, 3$. ΔR_{ij} and ΔT_{ij} ($i, j = 1, 2, 3; i < j$) describe the distance and time interval between the i^{th} signal and the j^{th} signal, respectively. It is worth noting that some invisible decay events are unable to exhibit the triple coincidence feature due to energy leakage, which is the loss of energy resulting from its deposition in non-active volumes. Conversely, some events yield a coincidence of more than three signals, for example, if two neutrons are captured or if radioactive isotopes are induced by energetic neutrons. The detection efficiencies for the four de-excitation modes in Eqs. (3.1)-(3.4) are 91.7%, 95.6%, 90.4%, and 90.5%. In order to better reflect the physical characteristics, we refer to the first, second, and third signals as prompt, delayed, and decay signals, respectively.

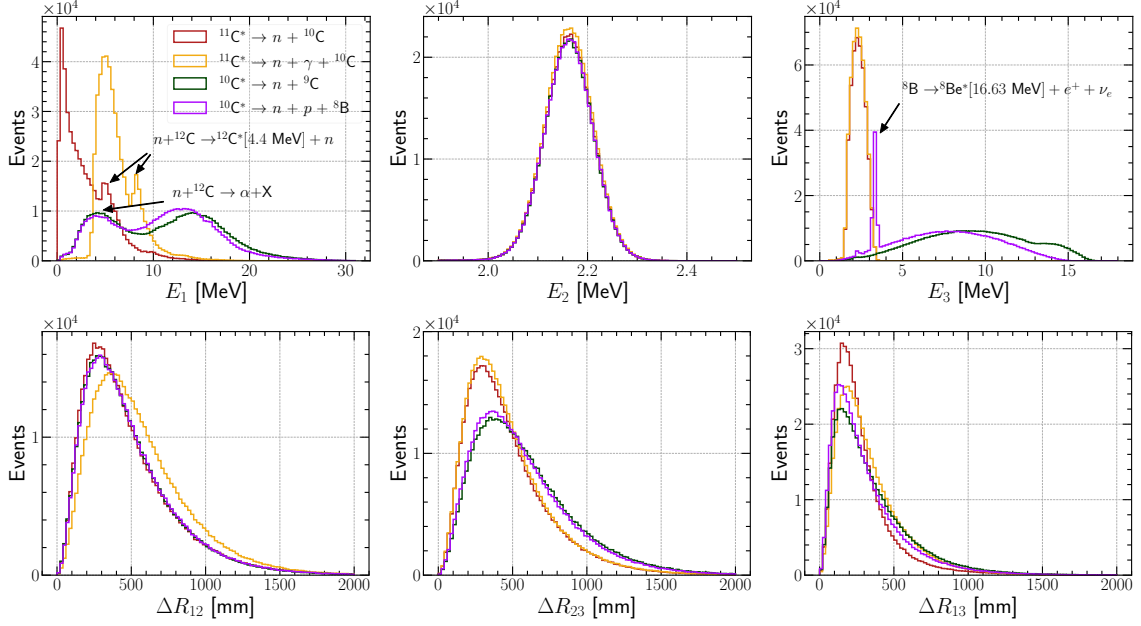


Figure 2. The E_1 , E_2 , E_3 , ΔR_{12} , ΔR_{13} , and ΔR_{23} distributions of four de-excitation modes.

The distributions of E_i and ΔR_{ij} from the four de-excitation modes in Eqs. (3.1)-(3.4) are displayed in Fig. 2. All prompt energy spectra exhibit two peaks because of the neutron elastic and inelastic scattering processes. For $^{11}\text{C}^* \rightarrow n + ^{10}\text{C}$ and $^{11}\text{C}^* \rightarrow n + \gamma + ^{10}\text{C}$, the higher energy peak of the E_1 distribution comes from the neutron inelastic scattering with ^{12}C , which emits a γ ray of 4.4 MeV. Due to the larger initial kinetic energy, neutrons from $^{10}\text{C}^* \rightarrow n + ^9\text{C}$ and $^{10}\text{C}^* \rightarrow n + p + ^8\text{B}$ can produce an α particle through the inelastic scattering $n + ^{12}\text{C} \rightarrow \alpha + \text{X}$, which corresponds to the lower energy peaks in the top-left panel of Fig. 2. For the decay signal, there is a very narrow peak around 3.3 MeV caused by the β^+ decay of $^8\text{B} \rightarrow ^8\text{Be}^* [16.63 \text{ MeV}] + e^+ + \nu_e$. This occurs because the excited state of $^8\text{Be}^*$ (16.63 MeV) will subsequently decay into two α particles, which has a large quenching factor in the LS. The spatial correlations of the triple coincidence signal show that the distances ΔR_{12} , ΔR_{13} and ΔR_{23} are mostly less than 1.5 m. It is worthwhile to stress that all distributions of E_i , ΔR_{ij} , and ΔT_{ij} from the MC simulation are in agreement with the expectations from the National Nuclear Data Center [34] and the International Atomic Energy Agency Nuclear Data Services [35].

3.2 Background sources

As discussed in the preceding subsection, the neutron invisible decays can generate a triple coincidence signal in the LS detector, which has been exploited by the KamLAND experiment to perform this search [15]. The dominant background stems from the doubly correlated IBD event ($p + \bar{\nu}_e \rightarrow e^+ + n$) followed by an uncorrelated natural radioactive decay. Unlike KamLAND, JUNO has a larger target mass and shallower rock overburden, potentially resulting in a wider variety of background sources. Therefore, we thoroughly investigate and simulate the various background sources, including IBD events, natural

radioactivity, cosmogenic isotopes, fast neutrons (FN), and atmospheric neutrino (Atm- ν) events. In Sec. 5, we will assess the JUNO background for the $n \rightarrow inv$ and $nn \rightarrow inv$ searches by leveraging these MC samples of background sources.

In JUNO [6, 7], the reactor antineutrinos are detected by the IBD reaction via the prompt-delayed coincidence signal. The kinetic energy deposited by the positron via ionization, together with its subsequent annihilation into typically two 0.511 MeV γ s, forms a prompt signal. The impinging neutrino transfers most of its energy to the positron. This establishes a strong correlation between the reconstructed energy of the positron and the energy of the antineutrino $\bar{\nu}_e$, which is a crucial parameter for measuring neutrino oscillations. The neutron is captured in an average time $\sim 220 \mu s$, and the corresponding photon emission forms a delayed signal. Neutron captures predominantly occur on hydrogen ($\sim 99\%$), resulting in the release of a single 2.2 MeV γ ray, while neutron captures on carbon ($\sim 1\%$) yield a gamma-ray signal with a total energy of 4.9 MeV, albeit very infrequently. The expected average IBD rate in JUNO is 57.4 /day [36]. The accidental coincidence between an IBD event and an uncorrelated single event significantly contributes to the background.

Natural radioactivity is found in all materials and can only be reduced by strict requirements for material screening and environmental control. It can be separated into internal radioactivity originating from the LS itself and external radioactivity from other parts of the JUNO detector, with the predominant external background originating in the PMT glass. The internal radioactivity primarily comes from radio-nuclides in the U/Th chains, with the assumed concentration of U/Th being 10^{-6} ppb [37]. They contribute to the deposited energy regardless of the type of emitted particles (α , β , and γ), as the energy is directly released into the LS, where these radionuclides are uniformly distributed. To reduce the impact of radioactivity, JUNO has implemented strict background control strategies, enabling the rate of natural radioactivity to be limited to 10 Hz. Ref. [37] provides a comprehensive summary of the approach taken by JUNO to achieve this goal and presents the internal and external radioactivity results from the detector simulation. The external radioactivity can be suppressed significantly with a fiducial volume cut of $R_i < 16.7$ m and an energy cut of 0.7–30 MeV as shown in Fig. 3. In this case, the internal and external radioactivity rates are around 1.98 Hz and 0.48 Hz. Meanwhile, the α particle from ^{238}U , ^{232}Th , ^{210}Po radioactive decay chains can interact with ^{13}C in LS, and the interaction of $^{13}\text{C}(\alpha, n)^{16}\text{O}$ may produce the prompt-delayed event. The expected rate of such events can be determined based on the concentrations [37] and neutron yields [38].

Cosmogenic radioactive isotopes and neutrons can be produced in the LS through the spallation of cosmic-ray muons. Approximately 3.94 Hz of muons will pass through the JUNO LS with an average energy of 207 GeV [7]. MUSIC [39] is employed to track muons traversing the rock to the underground experimental hall, based on the local geological map. Among the generated cosmogenic isotopes, the long-lived isotopes ^9Li and ^8He can undergo β^-n decay, which can mimic the prompt and delayed signals of neutron invisible decays. Other long-lived isotopes will give a single signal similar to natural radioactivity, which predominantly comes from ^{11}C , ^{12}B , ^6He , ^{10}C , and ^8Li . To address the observed discrepancies between the GEANT4 [29] simulation and actual isotope yield data, the

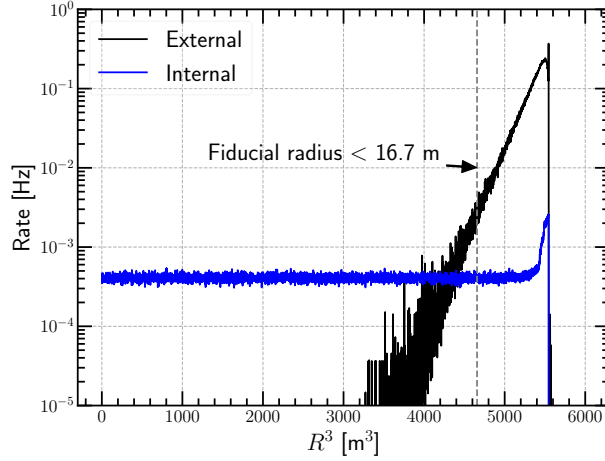


Figure 3. The internal and external natural radioactivity rates as a function of radius. The dashed line represents the fiducial radius.

cosmogenic isotope rates are adjusted based on the experimental results from both KamLAND [40] and Borexino [41]. The event rates for ${}^9\text{Li}$ and ${}^8\text{He}$ are determined to be 127 per day and 40 per day, while the event rates of ${}^{11}\text{C}$, ${}^{12}\text{B}$, ${}^6\text{He}$, ${}^{10}\text{C}$ and ${}^8\text{Li}$ are 50020, 2478, 2373, 953 and 705 per day, respectively. To enhance the precision of cosmogenic isotope results and study the muon veto strategy, we simulated a decade of muon data without including the photon production and propagation processes.

Fast neutrons, originating from untagged cosmic muons and coinciding with an uncorrelated single event, is another background that needs to be considered. The tagged efficiencies of muons passing through the LS and only the water buffer are almost 100% and 99.8% [6], respectively. The untagged muon is also called a rock muon, including the corner clipping muons and the muon whose track length in water is less than 50 cm. Fast neutrons associated with the untagged muons may enter the CD and produce a correlated signal, which can mimic the prompt and delayed signals, whose rate is ~ 0.4 /day. Note that the fast neutrons are primarily concentrated around the CD edge. Accordingly, the fiducial volume cut of $R_i < 16.7$ m lowers their rate to about 0.08 /day.

Atmospheric neutrino (Atm- ν) charged current (CC) and neutral current (NC) interactions can also contribute to the background of neutron invisible decays. Atm- ν CC events usually have an energy larger than the typical nuclear de-excitation energy [14]. For the prompt signal energy range from 0.7 to 30.0 MeV, the IBD-like event rate from the Atm- ν CC interaction has been estimated by Ref. [42]. It is evident that the IBD-like event rate is significantly lower than the JUNO reactor IBD rate. Here, we have found that the triple coincident events from Atm- ν CC reactions are negligible. An assessment of the expected CC and NC rates from atmospheric neutrinos below 100 MeV [43] resulted in a negligible contribution. Hence, our analysis primarily concentrates on NC background from atmospheric neutrinos with energies higher than 100 MeV. As listed in Table 2 of Ref. [44] and Table I of Ref. [45], the following three Atm- ν NC processes may directly

form a triple coincidence signal:

$$\nu/\bar{\nu} + {}^{12}\text{C} \rightarrow \nu/\bar{\nu} + n + {}^{11}\text{C} , \quad (3.5)$$

$$\nu/\bar{\nu} + {}^{12}\text{C} \rightarrow \nu/\bar{\nu} + 2n + {}^{10}\text{C} , \quad (3.6)$$

$$\nu/\bar{\nu} + {}^{12}\text{C} \rightarrow \nu/\bar{\nu} + 3p + n + {}^8\text{Li} , \quad (3.7)$$

where the daughter nuclei ${}^{11}\text{C}(\beta^+, 20.36 \text{ min}, 1.98 \text{ MeV})$, ${}^{10}\text{C}(\beta^+, 19.3 \text{ s}, 3.65 \text{ MeV})$ and ${}^8\text{Li}(\beta^-\alpha, 0.839 \text{ s}, 16.0 \text{ MeV})$ are radioactive. The reaction in Eq. (3.6) can produce only one neutron capture signal if one of two neutrons loses energy at the CD edge or disappears through the inelastic scattering with ${}^{12}\text{C}$. In addition to the three processes, some Atm- ν NC reactions can also form the triple signal indirectly through accidental coincidences between the prompt-delayed signal and an uncorrelated single event. The MC simulation indicates that over 90% of all prompt-delayed signals with $E_1 < 30 \text{ MeV}$ are generated by four dominant NC interactions:

$$\nu/\bar{\nu} + {}^{12}\text{C} \rightarrow \nu/\bar{\nu} + n + p + {}^{10}\text{B} , \quad (3.8)$$

$$\nu/\bar{\nu} + {}^{12}\text{C} \rightarrow \nu/\bar{\nu} + n + p + \alpha + {}^6\text{Li} , \quad (3.9)$$

$$\nu/\bar{\nu} + {}^{12}\text{C} \rightarrow \nu/\bar{\nu} + n + 2p + {}^9\text{Be} , \quad (3.10)$$

$$\nu/\bar{\nu} + {}^{12}\text{C} \rightarrow \nu/\bar{\nu} + n + p + d + {}^8\text{Be} . \quad (3.11)$$

Based on our estimation, the other Atm- ν NC reactions are negligible.

In this analysis, we consider the seven reactions in Eqs. (3.5)-(3.11) for the background analysis. The cross sections of these Atm- ν NC interactions can be obtained from the GENIE (3.0.6) [46] and NuWro (19.02) [47] generators. Both the GENIE and NuWro generators use physics models, which rely in different choices for the nuclear models, the axial mass M_A , the underlying reaction processes, and final state interaction (FSI) models. Determining the best model among the available options presents a significant challenge currently. Therefore, we use a total of five generator physics models to estimate the event rates of the seven NC processes with the help of the Atm- ν fluxes at the JUNO site [48]. The details of the generator models utilized in this study are presented in Table 1. For the de-excitation of the residual nuclei, we use the TALYS code [49] and take the same strategy as that of Refs. [42, 50]. Sec. 5.1 will explain how these different estimates are used to predict this background.

4 Event selection

To enhance JUNO's sensitivity to the neutron invisible decays, we should choose the proper event selection criteria to effectively suppress backgrounds while maintaining high signal efficiency. In this section, the muon veto strategy is first introduced before the event selection to reduce cosmogenic isotopes, radioactivity, and other backgrounds. Then, beyond the basic event selection criteria based on signal physical characteristics aimed at primarily selecting the vast majority of the neutron invisible decay events, a multiplicity cut strategy is designed to select real triple signals.

Table 1. Summary of generator models (G represents GENIE [46], N represents NuWro [47]) for atmospheric neutrino interactions. The Local Fermi Gas (LFG), Spectra Function (SF), and relativistic Fermi gas model with “Bodek-Ritchie” modifications (BRRFG) are used as the nuclear models, with M_A representing the axial mass. The Berger-Sehgal (BS) model is employed for the coherent and diffractive production (COH) and nuclear resonance production (RES). For the two particle two hole (2p2h), the empirical model is utilized for GENIE. Final state interactions are described by the hN, a traditional hadron-nucleon intranuclear cascade model, and hA, a custom model that offers a more empirical description of the effect of multiple hadron-nucleon interactions.

Models	version	M_A [GeV]	Nuclear Model	RES & COH	2p2h	FSI
G1	3.0.6	0.96	LFG	BS	empirical	hN
G2	3.0.6	0.96	LFG	BS	empirical	hA
G3	3.0.6	0.96	BRRFG	BS	empirical	hN
N1	19.02	1.03	SF	default	default	default
N2	19.02	1.03	LFG	default	default	default

4.1 Muon veto strategy

A muon veto must be used to reduce the impact of long-lived isotopes produced by the spallation of cosmic-ray muons in the JUNO LS [6]. Its primary goals are to maximize the rejection of ${}^9\text{Li}/{}^8\text{He}$ and to reduce triple coincidences produced through triple isotope production by the same muon, both of which are dominant backgrounds in the search for neutron invisible decays. JUNO has developed two kinds of muon veto strategies to investigate the reactor antineutrinos [36] and solar neutrinos [51]. Unlike the single signal from solar neutrinos and the prompt-delayed signal from reactor antineutrinos, a muon veto strategy tailored for the unique triple coincidence signal expected in this analysis is developed using a 10-year MC simulation as follows, based on the corresponding physical feature distribution:

- For all muons passing the water pool and/or the central detector, a veto of 3 ms after each muon is applied over the whole detector to suppress spallation neutrons and short-lived radioactive isotopes.
- For all muons passing the water pool and/or the central detector, a 3 m spherical volume around any spallation neutron candidates is vetoed for 30 s and 10 s in the $n \rightarrow inv$ and $nn \rightarrow inv$ analyses, respectively.
- For well-reconstructed muon tracks in the central detector caused by single or two far-apart (> 3 m) muons, a veto of 2 s is applied to candidate events with reconstructed vertices smaller than 2 m away from each track.
- For events containing two close and parallel muons (< 3 m), which constitute roughly 0.6% of muon-related events, a single track is often reconstructed. A cylindrical veto with a radius of 3.5 m around this track is applied for 5 s.

- For events where a track cannot be properly reconstructed, which amount to about 2% of all muon-related events and occur primarily when more than two muons go through the detector simultaneously, a 0.2 s veto is applied over the whole detector volume for $n \rightarrow inv$ due to its larger ΔT_{23} .

The above muon veto strategy can effectively reject the cosmogenic long-lived isotopes while keeping a high signal efficiency. For neutron invisible decay events, the dead time and dead volume introduced by the muon veto strategy may result in one of the signals in the triple signal being vetoed, leading to a decrease in the signal efficiency. The efficiencies of the four de-excitation modes in Eqs. (3.1)-(3.4) after the above muon veto are $65.7 \pm 0.2(\text{stat.})\%$, $65.5 \pm 0.2(\text{stat.})\%$, $80.8 \pm 0.2(\text{stat.})\%$, and $78.3 \pm 0.2(\text{stat.})\%$, respectively. Meanwhile, the long-lived cosmogenic isotopes and neutrons have been well suppressed. After applying the above muon veto strategy, the ${}^9\text{Li}$ and ${}^8\text{He}$ rates are approximately 0.07 (0.1) /day and 0.02 (0.06) /day for $n \rightarrow inv$ ($nn \rightarrow inv$). Compared with 127 /day and 40 /day before the muon veto, the ${}^9\text{Li}$ and ${}^8\text{He}$ rates have been reduced by a factor of over 500.

Table 2. Basic selection criteria used for $n \rightarrow inv$ and $nn \rightarrow inv$.

Quantity	$n \rightarrow inv$	$nn \rightarrow inv$
$R_{1,2,3}$ [m]	< 16.7	< 16.7
E_1 [MeV]	0.7-12	0.7-30
E_2 [MeV]	1.9-2.5	1.9-2.5
E_3 [MeV]	1.5-3.5	3.0-16.0
ΔT_{12} [ms]	< 1	< 1
ΔT_{23} [s]	0.002-100	0.002-3.0
ΔR_{12} [m]	< 1.5	< 1.5
ΔR_{23} [m]	< 1.5	< 1.5
ΔR_{13} [m]	< 1.0	< 1.0

4.2 Event selection

As previously mentioned, a fiducial volume cut of $R_i < 16.7$ m is chosen for both $n \rightarrow inv$ and $nn \rightarrow inv$ in order to reduce the contributions of external radioactivity and fast neutrons to backgrounds. As shown in Fig. 3, the fiducial radius cut can reject most external radioactivity events. According to the signal characteristics as demonstrated in Sec. 3.1, we set the basic event selection criteria for E_i , ΔR_{ij} , and ΔT_{ij} as listed in Table 2. For the $n \rightarrow inv$ and $nn \rightarrow inv$ analyses, the prompt energy E_1 is restricted to the range of [0.7, 12] MeV and [0.7, 30] MeV, respectively. For the delayed signal from the neutron capture, we require the reconstructed energy $E_2 \in [1.9, 2.5]$ MeV and the time interval of $\Delta T_{12} < 1.0$ ms. The decay energy E_3 from the daughter nuclei in Eqs. (3.1)-(3.4) takes the range of [1.5, 3.5] MeV ([3.0, 16.0] MeV) in the search of $n \rightarrow inv$ ($nn \rightarrow inv$). The corresponding time interval ΔT_{23} lies in the range [0.002, 100] s ([0.002, 3.0] s). To further

reduce the accidental coincidence backgrounds, the surviving triple signals are restricted to occur in proximity to each other: $\Delta R_{12} < 1.5$ m, $\Delta R_{23} < 1.5$ m, and $\Delta R_{13} < 1.0$ m. As shown in Fig. 2, these basic selection criteria can select the vast majority of the neutron invisible decay events.

Table 3. Summary of selection efficiencies (%) of four de-excitation modes for $n \rightarrow inv$ and $nn \rightarrow inv$.

Selection Criterion	$n \rightarrow inv$		$nn \rightarrow inv$	
	$^{11}\text{C}^* \rightarrow n + ^{10}\text{C}$	$^{11}\text{C}^* \rightarrow n + \gamma + ^{10}\text{C}$	$^{10}\text{C}^* \rightarrow n + ^9\text{C}$	$^{10}\text{C}^* \rightarrow n + p + ^8\text{B}$
All triple signals	100	100	100	100
Muon Veto	65.7 ± 0.2	65.5 ± 0.2	80.8 ± 0.2	78.3 ± 0.2
Fiducial Volume	83.5 ± 0.4	82.7 ± 0.4	82.9 ± 0.4	83.1 ± 0.4
Event Selection	75.4 ± 0.9	89.7 ± 0.3	89.2 ± 0.3	83.5 ± 0.3
Multiplicity Cut	93.8 ± 0.1	93.8 ± 0.1	$99.9 \pm \mathcal{O}(10^{-4})$	$99.9 \pm \mathcal{O}(10^{-4})$
Combined Selection	38.8 ± 0.5	45.6 ± 0.3	59.7 ± 0.4	54.3 ± 0.4

Applying the above selection criteria, we calculate the signal selection efficiencies of the four de-excitation modes in Eqs. (3.1)-(3.4) as listed in Table 3. The efficiency of the fiducial volume cut is about 83%, which is consistent with $(16.7/17.7)^3 \approx 84.0\%$. The selection criteria of E_i , ΔT_{ij} , and ΔR_{ij} preserve most of the signals. For $^{11}\text{C}^* \rightarrow n + ^{10}\text{C}$, the relatively small efficiency of 75.4% is due to the energy threshold of $E_1 > 0.7$ MeV, which can reduce some signals, as shown in the top-left panel of Fig. 2. For $^{10}\text{C}^* \rightarrow n + p + ^8\text{B}$, the requirement of $\Delta T_{23} < 3.0$ s rejects many ^8B decay signals because of its half-life time of 0.77 s. In Table 3, we present a summary of event selection efficiencies. According to Ref. [36], the systematic uncertainties are from the fiducial volume cut (2 cm vertex bias) and the event selection.

Most of the de-excitation events from Eqs. (3.1)-(3.4) will generate a triple coincidence signal in the JUNO LS. In reality, many single events from the natural radioactivity and cosmogenic isotopes can appear between the delayed and decay signals of neutron invisible decays, owing to the large time interval ΔT_{23} . In this case, the triple coincidence signal can easily form a quadruple or higher coincidence with an uncorrelated single event. To correctly select the triple coincidence signals from the experimental data and reject the influence of single events, this study uses two kinds of multiplicity cut methods. Method I first selects the prompt-delayed signal, which should satisfy the selection criteria of E_1 , E_2 , ΔR_{12} , and ΔT_{12} . In addition, we have the following requirements:

- No trigger with $0.7 < E < 12$ MeV in a 1 ms window before the prompt signal;
- No other events during ΔT_{12} ;
- No trigger with $0.7 < E < 12$ MeV in a 1 ms window before/after the decay signal;
- Only one prompt-delayed signal in a 100 s window before the decay signal.

Method II firstly searches for the neutron capture signal. Its requirements are the following:

- Only 1 satisfied trigger falls in $[-1, 0]$ ms;

- No other neutron capture signals within a spherical volume with a radius of 3 m during $[-3.001, 3.001]$ s;
- Only 1 satisfied trigger falls in $[0, 3]$ s.

The biggest difference is that Method I has a more strict space limit than Method II. It requires the absence of candidate signals that meet the criteria anywhere within the detector space, whereas Method II only requires no candidate signals within a specific selected spatial range. Hence, Method I gives a slightly lower multiplicity cut efficiency of 93.8 ± 0.1 ($97.9 \pm \mathcal{O}(10^{-2})$) compared to the 95.7 ± 0.1 ($99.9 \pm \mathcal{O}(10^{-4})$) of Method II for $n \rightarrow inv$ ($nn \rightarrow inv$). In the following parts of this work, we conservatively take Method I to analyze $n \rightarrow inv$ due to its larger time interval of ΔT_{23} . Method II is applied to $nn \rightarrow inv$.

Based on Table 3 and the detection efficiencies discussed in Sec. 3.1, we calculate the signal efficiencies of the four de-excitation modes in Eqs. (3.1)-(3.4) as listed in Table 4. The signal efficiencies ϵ_{n1} and ϵ_{n2} correspond to the de-excitation modes in Eqs. (3.1) and (3.2), while the signal efficiencies ϵ_{nn1} and ϵ_{nn2} correspond to those of Eqs. (3.3) and (3.4).

5 Background estimation

We have introduced all possible background sources in Sec. 3.2. Most backgrounds are formed by the accidental coincidence of two background sources, while the Atm- ν NC interactions can directly produce a triple coincidence signal. In this section, we estimate all types of backgrounds for $n \rightarrow inv$ and $nn \rightarrow inv$ based on the event selection criteria described in Sec. 4. Subsequently, the pulse shape discrimination technique and the multivariate analysis method will be employed to further suppress the background. For instance, for the IBD events followed by an uncorrelated single event, the prompt signals from neutron invisible decays and IBD events are generated by neutrons and positrons, respectively, which exhibit different pulse shapes [45, 52]. Consequently, the pulse shape discrimination (PSD) technique can be employed to reject background events. Furthermore, the correlations among E_1 , E_2 , E_3 , ΔR_{12} , ΔR_{23} , ΔR_{13} , ΔT_{12} , and ΔT_{23} exhibit variations between signal and accidental coincidence background. The discrepancies among the time, spatial and energy distributions suggest that the employment of the multivariate analysis (MVA) method will be instrumental in effectively discerning the signals from the backgrounds. To ensure the reliability of the results, we have employed two distinct background estimation methods and suppression techniques during the analysis that cross-validated each other. The background estimation utilizes both the MC approach and computational methods. For suppression methods, one approach does not integrate the PSD into the MVA, whereas the other incorporates the PSD as a variable along with the basic features. It is worth noting that these methodologies are employed for background analysis. In the ensuing sections, we have opted to elaborate on the method that exhibited very slightly superior performance for each decay mode.

5.1 $n \rightarrow inv$ analysis

To simplify, we refer to the prompt-delayed signal as a Double signal. Meanwhile, the events with no other correlated triggers are referred to as “Single”. We first estimate the Double+Single background rates ($R_{\text{Double+Single}}$), originating from the coincidence of a doubly correlated event (IBD, ${}^9\text{Li}/{}^8\text{He}$, ${}^{13}\text{C}(\alpha, n){}^{16}\text{O}$, fast neutron) with Single.

$$R_{\text{Double+Single}} = R_{\text{Double}}(1 - e^{-R_{\text{Single}} \cdot P_{(\Delta R_{23,13})} \cdot \Delta T_{23}}), \quad (5.1)$$

where R_{Double} is the rate of Double signals after applying the selection criteria of E_1 , E_2 , ΔR_{12} , ΔT_{12} , the fiducial volume cut, and the muon veto. $R_{\text{Single}} = 0.71$ Hz represents the Single rate with the energy E_3 in the range of [1.5, 3.5] MeV, including 0.64 Hz of radioactivity and 0.07 Hz of isotopes. $P_{(\Delta R_{23,13})}$ is the survival probability of backgrounds after the spatial cuts ΔR_{23} and ΔR_{13} .

After 10 years, the expected rates for this type of background, based on the spatial distribution of Single, are summarized in Table 4. Note that ${}^9\text{Li}/{}^8\text{He}$ +Single rates account for the possibility of both the correlated ${}^9\text{Li}/{}^8\text{He}$ events and the single event originating from the same muon shower. In Fig. 4, we show the energy, time interval, and spatial distributions of the IBD+Single background. As a comparison, we also plot the distributions of $n \rightarrow inv$, which is calculated based on the event selection in Sec. 4 and the sensitivity reported in Sec. 6, namely $\tau/B(n \rightarrow inv) = 5.0 \times 10^{31}$ yr. Using a similar method, the accidental triple coincidence from three Single has been estimated to be 1.46 ± 0.05 /10 years.

The systematic uncertainty of the IBD+Single rate arises from the uncertainties of both the IBD rate and the Single rate. Here we adopt a relative systematic uncertainty of 2% for the world reactor IBD rate based on Ref. [36]. For the Single rate, it consists of contributions from natural radioactivity and cosmogenic isotopes. The systematic uncertainty of the radioactivity rate is expected to be small, as we can measure the rate precisely after JUNO starts taking data. Therefore, a conservative uncertainty of 1% is used for the accidental rate [36]. For the cosmogenic isotopes rate, we assign a larger uncertainty of 20% according to the KamLAND experiment [40]. For the ${}^{13}\text{C}(\alpha, n){}^{16}\text{O}$, an uncertainty of 50% from Ref. [6] is applied.

For the Atm- ν NC background, we first calculate the total event rate of three interactions in Eqs. (3.5)-(3.7). The five typical generator models in Table 1 give significantly different predictions, as shown in Fig. 5. The rate derived from the NuWro SF nuclear model (N2) is lower compared to other models. The averaged rate from the three GENIE models is higher than that from the two NuWro models. To reasonably estimate the Atm- ν NC background, we select the maximal and minimal values among the five predicted event rates, and then take their mean value as the nominal event rate. The systematic uncertainty from the interaction cross section is chosen as half of the difference between the maximum and minimum values. This uncertainty estimation method can fully encompass all five models. Using Eq. (5.1), we analyze the accidental coincident background between the Atm- ν NC reactions in Eqs. (3.8)-(3.11) and Single. All five models indicate that the Atm- ν NC Double+Single background is not negligible for $n \rightarrow inv$, as shown in Fig. 5.

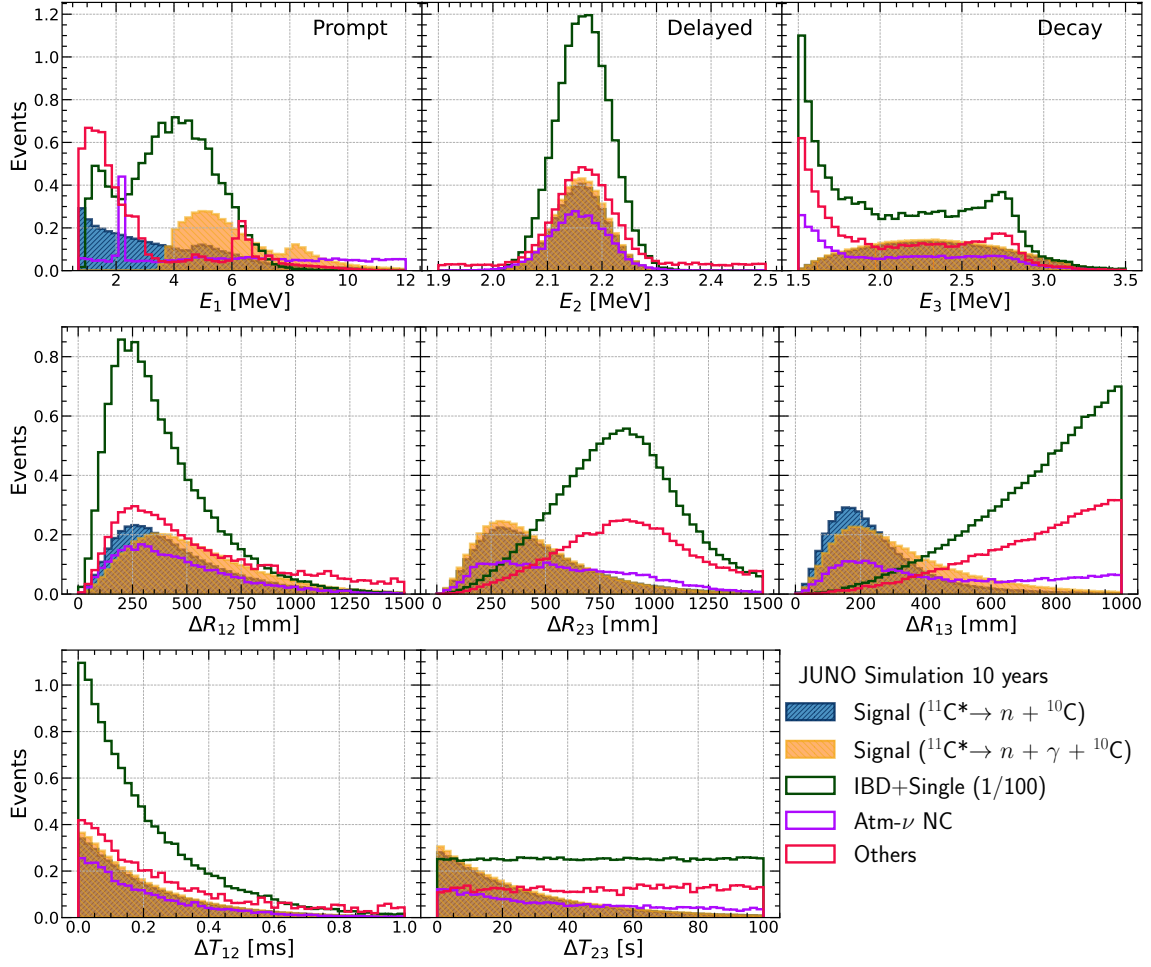


Figure 4. The E_1 , E_2 , E_3 , ΔR_{12} , ΔR_{13} , ΔR_{23} , ΔT_{12} , and ΔT_{23} distributions of $n \rightarrow inv$ and backgrounds. The vertical axis represents the event number over a period of 10 years, and x-axis for each plot corresponds to the selection criterion in Table 2. The expected signal number is calculated based on the JUNO sensitivity of this article, namely $\tau/B(n \rightarrow inv) = 5.0 \times 10^{31}$ yr. The number in parentheses in the legend represents the scale factor.

We finally consider the statistical error and the systematic uncertainty from the Atm- ν flux. Previous research has already delineated the systematic uncertainty estimation from the Atm- ν flux at the JUNO site [50]. Given that this research also employs the identical Honda Flux with an energy range of 0.1-20 GeV, we conservatively apply a systematic uncertainty of 30% to the flux. After considering all uncertainties, the final total Atm- ν NC background number is 3.0 ± 1.1 in 10 years, as listed in Table 4. Their energy, time interval, and spatial distributions have been shown in Fig. 4. In the E_1 spectrum of NC, a peak is observed from the $2n+^{10}\text{C}$ reaction channel. Our simulation observed a case where some final state nucleons of the NC interaction process from GENIE had zero momentum in GENIE (3.0.6), potentially affecting the prompt signal composition for $2n+^{10}\text{C}$. Additional calculations were performed to address this issue. Our estimations with 5 models and 2

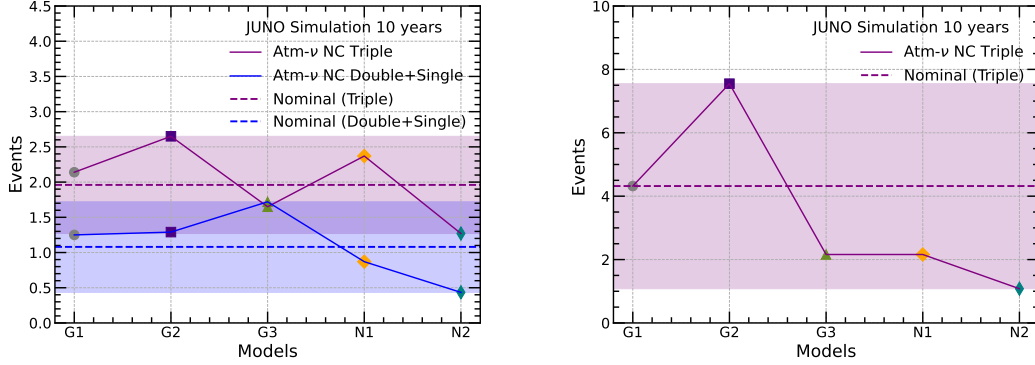


Figure 5. The Atm- ν NC background rates from five typical generator models in Table 1 after basic event selection criteria for $n \rightarrow inv$ (left) and $nn \rightarrow inv$ (right). The horizontal axis describes different models, while the vertical axis represents the background rate per 10 years. The dashed line within the corresponding color rectangular region denotes the average of the maximum and minimum among five models, which we take as the nominal background rate. Its systematic uncertainty is chosen as half of the difference between the maximal and minimal values.

generators (GENIE and NuWro) show that its impact on the final results is negligible.

After the basic event selections, many backgrounds still remain, as listed in Table 4, especially from IBD+Single. The prompt signal for the vast majority of background events is caused by a positron. However, the neutron invisible decays generate the prompt signal through the neutron elastic and inelastic scattering processes as described in Sec. 3.1. Note that the deposited energies of positrons and energetic neutrons in the LS have distinct photon emission time profiles [45, 52]. Based on this feature, JUNO is planning to use the PSD technique described in [42, 53] to separate the IBD events from the Atm- ν NC events. Here we primarily utilize the same PSD tool to distinguish the prompt signal of the neutron invisible decays and two kinds of dominant backgrounds (IBD+Single, ^9Li +Single). As shown in the left panel of Fig. 6, the PSD technique can effectively identify the invisible decay signals from the two backgrounds, especially from the IBD+Single. There is a tail around a PSD value of 1.0 for ^9Li events, which can be attributed to the fact that the prompt signal of ^9Li contains the kinetic energy of both the β^- and neutron. Note that the Atm- ν NC background cannot be suppressed effectively since its prompt signal also comes from the energetic neutrons.

In addition to the PSD technique, some significant differences between the signals and backgrounds can be clearly observed in Fig. 4. These differences among the time, space, and energy distributions imply that the multivariate analysis method can be powerful in further separating the signal from the background. Here we employ the Boosted Decision Trees (BDT) and consider eight input variables, including E_1 , E_2 , E_3 , ΔR_{12} , ΔR_{23} , ΔR_{13} , ΔT_{12} , and ΔT_{23} . The right panel of Fig. 6 shows the BDT output distributions. It is clear that the MVA method can reject most backgrounds except for the Atm- ν NC triple events. Applying the PSD and MVA methods, the residual backgrounds and the signal efficiency are derived as tabulated in Table 4. The cut values for the PSD and BDT values have been

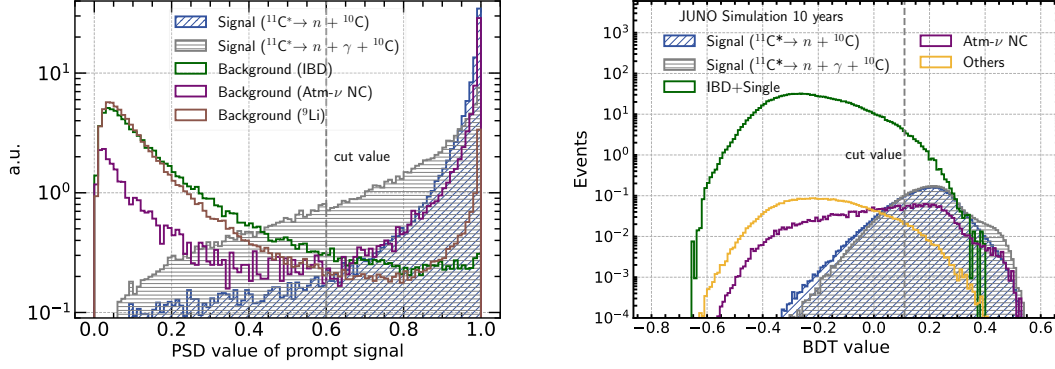


Figure 6. The PSD (left) and MVA (right) separation capabilities for $n \rightarrow inv$. The left plot is normalized to unity to highlight the performance of the PSD, while right plot shows the BDT performance and the vertical axis represents the event number over a period of 10 years.

chosen as 0.60 and 0.11 for the best sensitivity, respectively. The chosen values correspond to the BDT and PSD at the optimum ϵ_{sig}/S_{90} , where S_{90} represents the average upper limit of the signal number at a 90% confidence level. Further details of the optimization can be found in the appendix. The IBD+Single background is significantly suppressed relative to the Atm- ν NC background. This is because of the inherent dissimilarity in PSD values between the IBD events and the signals. The IBD+Single and Atm- ν NC events contribute predominantly to the backgrounds after PSD+MVA suppression, with the other backgrounds contributing negligibly.

5.2 $nn \rightarrow inv$ analysis

To ensure the reliability of the results, we have developed two independent approaches to estimate the backgrounds for both $n \rightarrow inv$ and $nn \rightarrow inv$. In contrast with the approach described in Sec. 5.1 for $n \rightarrow inv$ analysis, we employed a numerical calculation approach to estimate the background of $nn \rightarrow inv$. For the Double+Single background, we first divide the fiducial sphere of radius 16.7 m into 4658 concentric shells of equal volume due to the non-uniform radial distribution of external radioactivity, and assume the single events are uniformly distributed in each shell. Secondly, due to the selection criteria of $\Delta R_{12} < 1.5$ m and $\Delta R_{23} < 1.5$ m, a spherical volume with a radius of 1.5 m is chosen around the delayed signal. For a prompt-delayed event in the i^{th} shell, we can calculate the fraction f_i^j of the volume of the j^{th} shell inside this sphere to the total volume of this shell. Finally, we use the following formula to calculate the background rate of the Double+Single events:

$$R_{\text{Double+Single}} = \sum_{i=1} R_{\text{Double}}^i (1 - e^{-\sum_j f_i^j \cdot R_{\text{Single}}^j \Delta T_{23}}) P_{\Delta R_{13}}, \quad (5.2)$$

where R_{Double}^i is the prompt-delayed event rate in the i^{th} shell after applying the selection criteria of E_1 , E_2 , ΔR_{12} , ΔT_{12} , the fiducial volume cut, and the muon veto strategy. Similarly, R_{Single}^j denotes the Single rate in the j^{th} shell following the $3.0 \text{ MeV} < E_3 < 16.0 \text{ MeV}$ selection. $P_{\Delta R_{13}}$ is the survival probability of backgrounds after the ΔR_{13} cut.

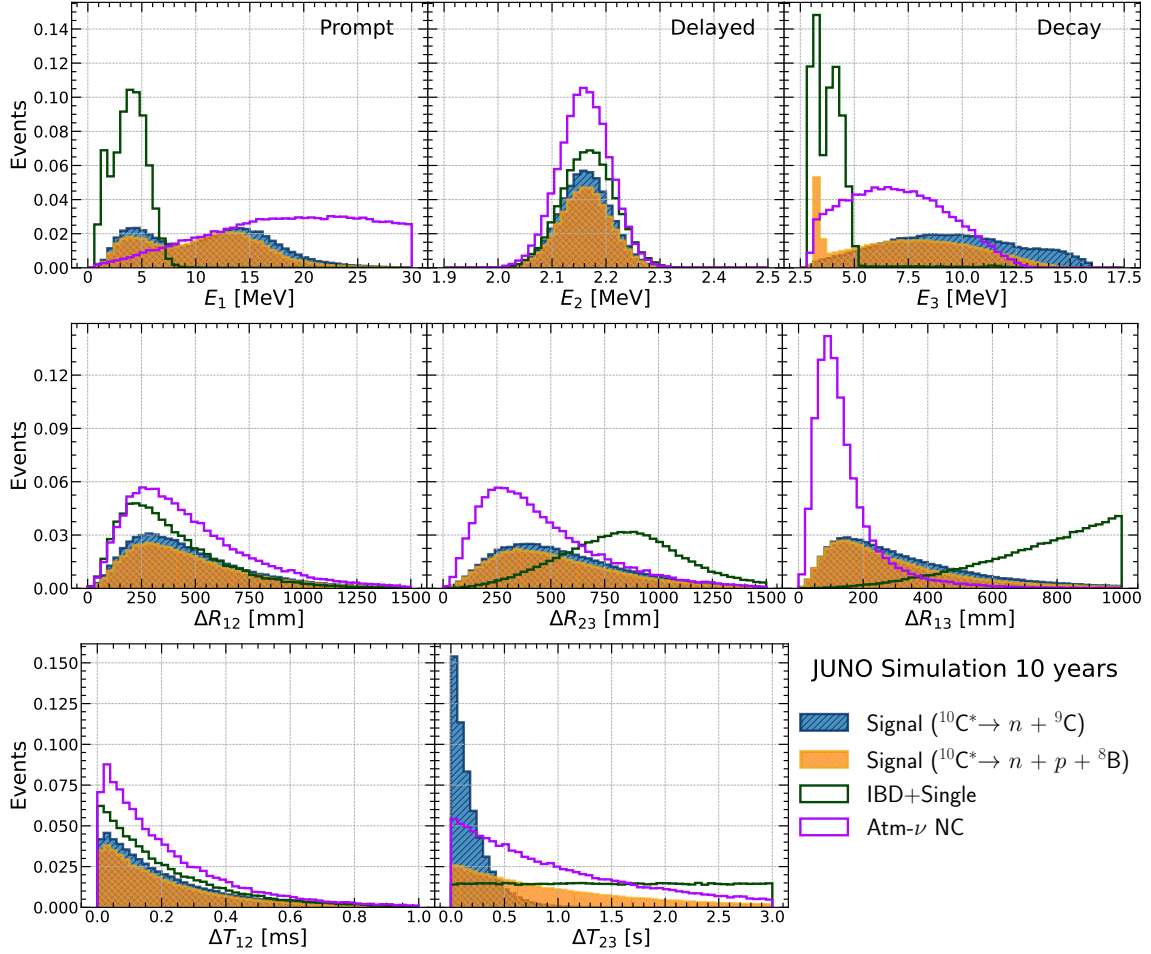


Figure 7. The E_1 , E_2 , E_3 , ΔR_{12} , ΔR_{13} , ΔR_{23} , ΔT_{12} , and ΔT_{23} distributions of $nn \rightarrow inv$ and two dominant backgrounds. The vertical axis represents the event number over a period of 10 years, and x-axis for each plot corresponds to the selection criterion in Table 2. The expected signal number is calculated based on the JUNO sensitivity of this article, namely $\tau/B(nn \rightarrow inv) = 1.4 \times 10^{32}$ yr.

By utilizing the event rates of R_{Double}^i and R_{Single}^j in each shell, we estimate the background rates from the Double+Single. It is found that the expected number of IBD+Single event is 3.01 ± 0.09 in 10 years. In Fig. 7, we plot the energy, time interval, and spatial distributions of the IBD+Single background, where the signal distributions are calculated based on the event selection in Sec. 4 and the JUNO sensitivity of $\tau/B(n \rightarrow inv) = 1.4 \times 10^{32}$ yr in this work. Note that other Double+Single backgrounds from ${}^9\text{Li}/{}^8\text{He}$, ${}^{13}\text{C}(\alpha, n){}^{16}\text{O}$ and fast neutrons, and the accidental triple coincidence of three Single are negligible. Besides the accidental coincidence with Single, ${}^9\text{Li}/{}^8\text{He}$ can also form a triple coincidence event with an isotope from the same muon shower. Based on the 10 years of simulation data of cosmic muons, we find that the final rate of this kind of background is 0.13 ± 0.13 per 10 years. A relative statistical uncertainty of 100% has been assigned.

For $nn \rightarrow inv$, one can easily find that the Atm- ν NC Double+Single background

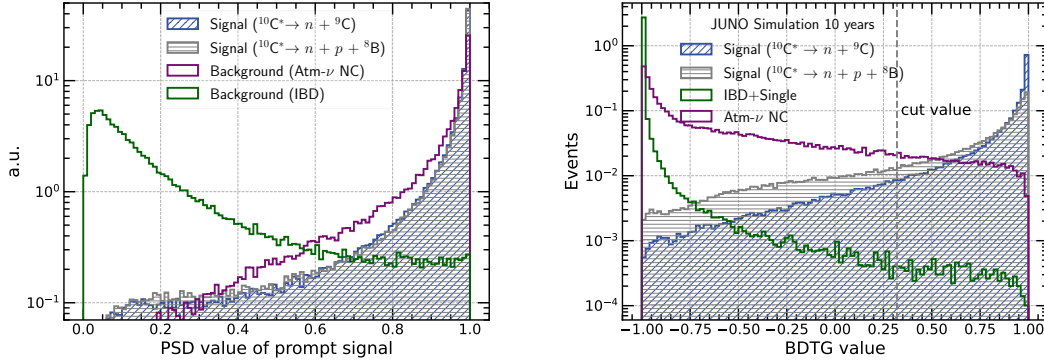


Figure 8. The PSD (left) and MVA (right) separation capabilities for $nn \rightarrow inv$. The left plot is normalized to unity to highlight the performance of the PSD, while right plot show the BDTG performance and the vertical axis represents the event number over a period of 10 years.

rate (0.1/10 years) will be negligible compared to the IBD+Single rate. Consequently, we focus exclusively on the Atm- ν NC triple coincident events in Eqs. (3.5)-(3.7). In fact, the dominant channel is $\nu/\bar{\nu} + {}^{12}\text{C} \rightarrow \nu/\bar{\nu} + 3p + n + {}^8\text{Li}$. This is because the selection criteria of $3.0 \text{ MeV} < E_3 < 16.0 \text{ MeV}$ can reject all ${}^{11}\text{C}$ and most of ${}^{10}\text{C}$. In addition, $\Delta T_{23} < 3.0 \text{ s}$ can also remove many ${}^{10}\text{C}$ since its half-life is 19.29 s. Here, we still employ five generator models to estimate the rate of Atm- ν NC triple events, as shown in Fig. 5. Using the same uncertainty estimation method in Sec. 5.1, the Atm- ν NC background rate is given by 4.3 ± 3.5 in 10 years, including both the cross section and flux uncertainties. The energy, time interval, and spatial distributions of the Atm- ν NC background have also been illustrated in Fig. 7.

After the basic event selections, the estimated total background rate is 7.4 ± 3.5 per 10 years, as listed in Table 4. Here, we further suppress these backgrounds by using the PSD and MVA methods. As shown in the left panel of Fig. 8, the PSD technique can also effectively distinguish the invisible decay signals from the IBD+Single background. To enhance the reliability of our results, the $nn \rightarrow inv$ analysis incorporates some differences compared to $n \rightarrow inv$, such as the incorporation of the PSD value into the MVA and the use of a BDT with Gradient Boosting (BDTG). We take the PSD output, along with other basic features, as an input variable for the MVA training. Whereas PSD and MVA are treated as two independent variables for the $n \rightarrow inv$ analysis. In the right panel of Fig. 8, we plot the MVA output distribution for $nn \rightarrow inv$. It indicates that this MVA method has a good capability to distinguish the signal from the IBD+Single and Atm- ν NC backgrounds. In the following analyses, the BDTG cut value of 0.32 is chosen to maximize the sensitivity. Further optimization details are provided in the appendix. In this case, the residual background rates and signal efficiencies after PSD+MVA have been listed in Table 4. The Atm- ν NC events and the ${}^9\text{Li}/{}^8\text{He}$ +Single become the dominant backgrounds after PSD+MVA suppression. It is worth emphasizing that the IBD+Single background is suppressed to a negligible level.

Table 4. Summary of the background event rates (10 years) and signal efficiencies before and after the PSD+MVA for $n \rightarrow inv$ and $nn \rightarrow inv$.

Backgrounds (10 years)	$n \rightarrow inv$		$nn \rightarrow inv$	
	Basic selection	PSD + MVA	Basic selection	PSD + MVA
IBD + Single	1235 ± 50	2.72 ± 0.10	3.01 ± 0.09	0.0110 ± 0.0003
Atm- ν NC	3.0 ± 1.1	0.89 ± 0.67	4.3 ± 3.5	0.55 ± 0.63
$^{13}\text{C}(\alpha, n)^{16}\text{O}$ + Single	3.4 ± 1.4	0.036 ± 0.013	–	–
$^9\text{Li}/^8\text{He}$ + Single	1.55 ± 0.39	0.29 ± 0.17	0.13 ± 0.13	0.13 ± 0.13
Accidental	1.46 ± 0.05	0.095 ± 0.004	–	–
Total	1244 ± 50	4.03 ± 0.70	7.4 ± 3.5	0.69 ± 0.64
Signal efficiency (%)	$n \rightarrow inv$		$nn \rightarrow inv$	
	Basic selection	PSD + MVA	Basic selection	PSD + MVA
$\epsilon_{n(nn)1}$	35.6 ± 0.2	23.5 ± 0.2	54.0 ± 0.3	48.2 ± 0.3
$\epsilon_{n(nn)2}$	43.6 ± 0.3	30.3 ± 0.3	49.2 ± 0.3	36.3 ± 0.3

6 Sensitivity

Based on the MC simulation, the background rates, signal efficiencies, and their uncertainties have been derived as listed in Table 4. The JUNO sensitivity for $n \rightarrow inv$ can be calculated as follows:

$$\tau/B(n \rightarrow inv) > N_0 T \sum_{i=1,2} \epsilon_{ni} B_{ni}/S_{90} , \quad (6.1)$$

where $B(n \rightarrow inv)$ represents the branching ratio of the invisible decay mode $n \rightarrow inv$ when one neutron undergoes the baryon number-violating decay. $N_0 = 1.76 \times 10^{33}$ is the number of s -shell neutrons, and T is the JUNO running time. The signal efficiencies ϵ_{ni} can be found in Table 4. $B_{n(nn)i}$ are the de-excitation branching ratios for single (two) neutron invisible decay, which can be known from Eqs. (3.1)-(3.4). A systematic uncertainty of 30% will be considered, stemming from the theoretical prediction of de-excitation branching ratios of highly excited residual nuclei [14]. S_{90} is the upper limit of the detected signal number at a 90% confidence level (C.L.). It depends on the number of observed events and the background level. For $nn \rightarrow inv$, the calculation of sensitivity follows a similar procedure but with corresponding s -shell nn pairs number of $N_0 = 8.8 \times 10^{32}$, signal efficiencies ϵ_{nni} and branching ratios B_{nni} .

The likelihood contours method [54] (usually denoted as the Feldman-Cousins method) is employed to calculate S_{90} for $n \rightarrow inv$ and $nn \rightarrow inv$. Here we report the sensitivities using the average upper limits, which are obtained by the following formula [55]:

$$S_{90} = \sum_{n=0}^{\infty} P(n|b) U(n|b), \quad (6.2)$$

where $U(n|b)$ is a function yielding the upper limit for a given observation n and a predicted background b through the likelihood contours method in 90% confidence level. $P(n|b)$ is the

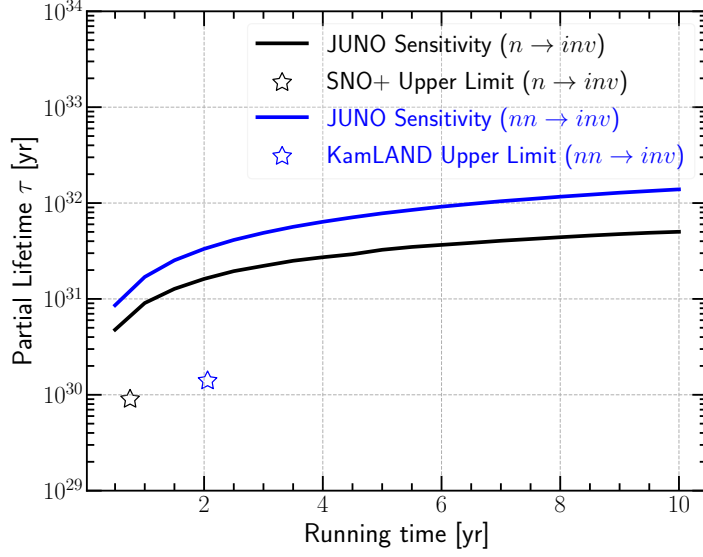


Figure 9. JUNO sensitivities to $n \rightarrow inv$ and $nn \rightarrow inv$ as a function of the running time at 90% C.L.. SNO+ and KamLAND give the current best upper limits in the search of $n \rightarrow inv$ and $nn \rightarrow inv$ based on experimental data, respectively.

Poisson distribution for the pure background. The systematic uncertainties in signal efficiency and backgrounds are accounted for by integrating over probability density functions that parametrize these uncertainties [56]. The large background uncertainty in $nn \rightarrow inv$ may lead to a negative value when assuming a Gaussian distribution. Thus, we choose the Log-Normal distribution [56] to describe the uncertainties of the background rate. The signal efficiencies, background rates, and their uncertainties, as shown in Table 4, result in the following JUNO sensitivities to $n \rightarrow inv$ and $nn \rightarrow inv$ after 10 years of data taking at the 90% C.L.:

$$\begin{aligned} \tau/B(n \rightarrow inv) &> 5.0 \times 10^{31} \text{ years}, \\ \tau/B(nn \rightarrow inv) &> 1.4 \times 10^{32} \text{ years}. \end{aligned} \tag{6.3}$$

The predicted sensitivity of $n \rightarrow inv$ ($nn \rightarrow inv$) is almost one(two) orders of magnitude better than the SNO+ (KamLAND) results. In Fig. 9, we plot the JUNO sensitivity as a function of the running time. It is found that with two years of data, JUNO will give an order of magnitude improvement compared with the current best limits: $\tau/B(n \rightarrow inv) > 9.0 \times 10^{29} \text{ yr}$ and $\tau/B(nn \rightarrow inv) > 1.4 \times 10^{30} \text{ yr}$.

To ensure the reliability of the results in Eq. (6.3), we use the analysis method in Sec. 5.1 (Sec. 5.2) and the corresponding multiplicity cut strategy to study $nn \rightarrow inv$ ($n \rightarrow inv$). It is found that different analysis methods only slightly influence the final sensitivities. In addition, we have also varied the MVA cuts to investigate the sensitivity changes. The predicted sensitivities are not significantly affected by the MVA cut value when it falls within the range of $[0, 0.5]$. To assess the impact of Atm- ν NC as the main

background on the predicted sensitivities, we enlarge their nominal values and uncertainties. We observe that for both decay modes, escalating the Atm- ν NC uncertainty to 150% marginally affects the predicted sensitivities. Given that Atm- ν NC is one of the main backgrounds for both analyses, the sensitivity is expected to change by about 10% and 20% when doubling the nominal value of the Atm- ν NC event rate, respectively.

7 Conclusion

In conclusion, we have investigated neutron invisible decays in the JUNO LS detector. The triple coincidence characteristic arising from the invisible decays of s -shell neutrons in ^{12}C has been briefly described, providing insight into the development of dedicated selection criteria applied to the signal sample generated with the full simulation. To correctly select triple coincidence signals from the experimental data and minimize the influence of the uncorrelated single signals, we have developed two muon veto strategies and implemented two types of multiplicity cut methods tailored to the characteristics of both the signal and backgrounds. On the other hand, we have conducted a detailed estimation of all potential backgrounds, which have been classified into six categories: IBD+Single, Isotope($^9\text{Li}/^8\text{He}$)+Single, FN+Single, $^{13}\text{C}(\alpha, n)^{16}\text{O}$ +Single, Accidental backgrounds, and Atm- ν NC events. It is observed that the IBD+Single and Atm- ν NC events are the dominant backgrounds. To suppress backgrounds further, we employ pulse shape discrimination and multivariate analysis techniques in both searches. After 10 years of JUNO data taking, the expected background numbers for $n \rightarrow inv$ and $nn \rightarrow inv$ are 4.07 ± 0.68 and 0.69 ± 0.64 , with final signal efficiencies of 26.7% and 42.3%, respectively. Finally, we have found that with two years of data, JUNO will yield an improvement by an order of magnitude with respect to the current best limits. After 10 years of data taking, the expected sensitivities for JUNO are $\tau/B(n \rightarrow inv) > 5.0 \times 10^{31} \text{ yr}$ and $\tau/B(nn \rightarrow inv) > 1.4 \times 10^{32} \text{ yr}$ at the 90% confidence level.

Acknowledgement

We are grateful for the ongoing cooperation from the China General Nuclear Power Group. This work was supported by the Chinese Academy of Sciences, the National Key R&D Program of China, the CAS Center for Excellence in Particle Physics, Wuyi University, and the Tsung-Dao Lee Institute of Shanghai Jiao Tong University in China, the Institut National de Physique Nucléaire et de Physique de Particules (IN2P3) in France, the Istituto Nazionale di Fisica Nucleare (INFN) in Italy, the Italian-Chinese collaborative research program MAECI-NSFC, the Fond de la Recherche Scientifique (F.R.S-FNRS) and FWO under the “Excellence of Science – EOS” in Belgium, the Conselho Nacional de Desenvolvimento Científico e Tecnológico in Brazil, the Agencia Nacional de Investigacion y Desarrollo in Chile, the Charles University Research Centre and the Ministry of Education, Youth, and Sports in Czech Republic, the Deutsche Forschungsgemeinschaft (DFG), the Helmholtz Association, and the Cluster of Excellence PRISMA+ in Germany, the Joint Institute of Nuclear Research (JINR) and Lomonosov Moscow State University in Russia, the joint

Russian Science Foundation (RSF) and National Natural Science Foundation of China (NSFC) research program, the MOST and MOE in Taiwan, the Chulalongkorn University and Suranaree University of Technology in Thailand, and the University of California at Irvine in USA.

Appendix: Optimization of sensitivity

We separately studied the ϵ_{sig}/S_{90} variation trends with the BDT/PSD and BDTG cut values for two invisible decay modes, as shown in the following Fig. 10. The left panel depicts the case of $n \rightarrow inv$, where a two-dimensional scan was performed using PSD and BDT values, with the white star indicating the location of the optimal scan value. For $nn \rightarrow inv$, as PSD is used as an input variable for BDTG, it can be represented by a one-dimensional curve. Similarly, the red star represents the optimal scan point. It should be noted that, in order to simplify the calculation during the optimization process, the systematic uncertainties of signal efficiency and background event counts were not taken into account.

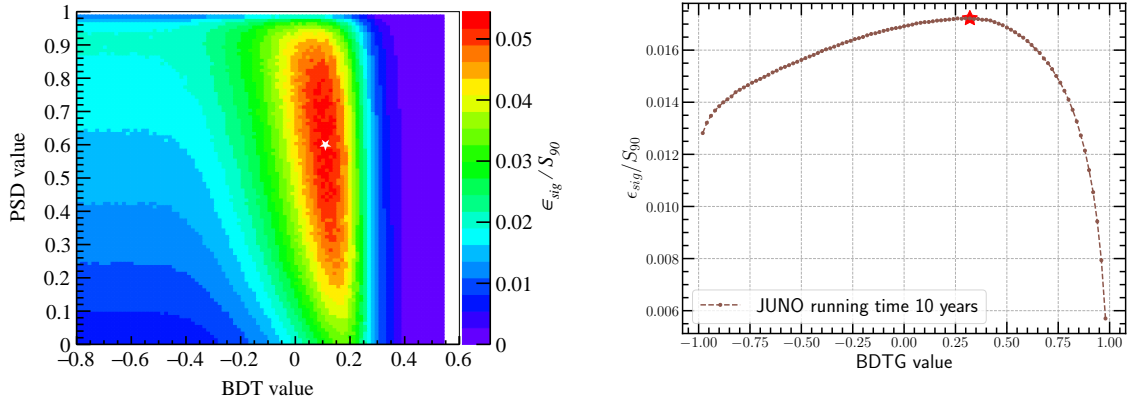


Figure 10. The sensitivity (without including systematic uncertainty) variation trends with the BDT/PSD cuts of $n \rightarrow inv$ (Left) and the BDTG cut of $nn \rightarrow inv$ (Right). The white star and red star in the graph represent the optimal value for $n \rightarrow inv$ and $nn \rightarrow inv$, respectively.

References

- [1] A.D. Sakharov, *Violation of CP Invariance, C asymmetry, and baryon asymmetry of the universe*, *Pisma Zh. Eksp. Teor. Fiz.* **5** (1967) 32.
- [2] P. Nath and P. Fileviez Perez, *Proton stability in grand unified theories, in strings and in branes*, *Phys. Rept.* **441** (2007) 191 [[hep-ph/0601023](#)].
- [3] PARTICLE DATA GROUP collaboration, *Review of particle properties*. Particle Data Group, *Phys. Rev. D* **50** (1994) 1173.
- [4] Particle Data Group, *Review of Particle Physics*, *PTEP* **2022** (2022) 083C01.

- [5] Super-Kamiokande collaboration, *First gadolinium loading to Super-Kamiokande*, *Nucl. Instrum. Meth. A* **1027** (2022) 166248 [[2109.00360](#)].
- [6] JUNO collaboration, *Neutrino Physics with JUNO*, *J. Phys. G* **43** (2016) 030401 [[1507.05613](#)].
- [7] JUNO collaboration, *JUNO physics and detector*, *Prog. Part. Nucl. Phys.* **123** (2022) 103927 [[2104.02565](#)].
- [8] JUNO collaboration, *JUNO Conceptual Design Report*, [1508.07166](#).
- [9] Hyper-Kamiokande collaboration, *Hyper-Kamiokande Design Report*, [1805.04163](#).
- [10] DUNE collaboration, *Long-Baseline Neutrino Facility (LBNF) and Deep Underground Neutrino Experiment (DUNE): Conceptual Design Report, Volume 2: The Physics Program for DUNE at LBNF*, [1512.06148](#).
- [11] T.M. Undagoitia, F. von Feilitzsch, M. Goger-Neff, C. Grieb, K.A. Hochmuth, L. Oberauer et al., *Search for the proton decay $p \rightarrow \bar{\nu}K^+$ in the large liquid scintillator low energy neutrino astronomy detector LENA*, *Phys. Rev. D* **72** (2005) 075014 [[hep-ph/0511230](#)].
- [12] KamLAND collaboration, *Search for the proton decay mode $p \rightarrow \bar{\nu}K^+$ with KamLAND*, *Phys. Rev. D* **92** (2015) 052006 [[1505.03612](#)].
- [13] JUNO collaboration, *JUNO Sensitivity on Proton Decay $p \rightarrow \bar{\nu}K^+$ Searches*, *Chin. Phys. C* **47** (2023) 113002 [[2212.08502](#)].
- [14] Y.A. Kamyshev and E. Kolbe, *Signatures of nucleon disappearance in large underground detectors*, *Phys. Rev. D* **67** (2003) 076007 [[nucl-th/0206030](#)].
- [15] KamLAND collaboration, *Search for the invisible decay of neutrons with KamLAND*, *Phys. Rev. Lett.* **96** (2006) 101802 [[hep-ex/0512059](#)].
- [16] K.S. Babu et al., *Working Group Report: Baryon Number Violation*, in *Snowmass 2013: Snowmass on the Mississippi*, 11, 2013 [[1311.5285](#)].
- [17] Super-Kamiokande collaboration, *Search for proton decay via $p \rightarrow \nu K^+$ using 260 kiloton-year data of Super-Kamiokande*, *Phys. Rev. D* **90** (2014) 072005 [[1408.1195](#)].
- [18] R.N. Mohapatra and A. Perez-Lorenzana, *Neutrino mass, proton decay and dark matter in TeV scale universal extra dimension models*, *Phys. Rev. D* **67** (2003) 075015 [[hep-ph/0212254](#)].
- [19] D. Barducci, M. Fabbrichesi and E. Gabrielli, *Neutral Hadrons Disappearing into the Darkness*, *Phys. Rev. D* **98** (2018) 035049 [[1806.05678](#)].
- [20] S. Girmohanta and R. Shrock, *Baryon-Number-Violating Nucleon and Dinucleon Decays in a Model with Large Extra Dimensions*, *Phys. Rev. D* **101** (2020) 015017 [[1911.05102](#)].
- [21] S. Girmohanta, *Nucleon and dinucleon decays to leptonic final states in a left-right symmetric model with large extra dimensions*, *Eur. Phys. J. C* **81** (2021) 143 [[2005.12952](#)].
- [22] SNO+ collaboration, *Improved search for invisible modes of nucleon decay in water with the SNO+detector*, *Phys. Rev. D* **105** (2022) 112012 [[2205.06400](#)].
- [23] JUNO, Daya Bay collaboration, *Optimization of the JUNO liquid scintillator composition using a Daya Bay antineutrino detector*, *Nucl. Instrum. Meth. A* **988** (2021) 164823 [[2007.00314](#)].

- [24] JUNO collaboration, *Mass testing and characterization of 20-inch PMTs for JUNO*, *Eur. Phys. J. C* **82** (2022) 1168 [2205.08629].
- [25] JUNO collaboration, *The JUNO experiment Top Tracker*, *Nucl. Instrum. Meth. A* **1057** (2023) 168680 [2303.05172].
- [26] JUNO collaboration, *Calibration Strategy of the JUNO Experiment*, *JHEP* **03** (2021) 004 [2011.06405].
- [27] K. Zhu, Y. Guo, Z. Cai, Y. Liu, F. Zhang, Y. Meng et al., *Verification of the calibration method for the boundary effect in JUNO*, *JINST* **17** (2022) P10024.
- [28] T. Lin et al., *Simulation software of the JUNO experiment*, *Eur. Phys. J. C* **83** (2023) 382 [2212.10741].
- [29] GEANT4 collaboration, *GEANT4—a simulation toolkit*, *Nucl. Instrum. Meth. A* **506** (2003) 250.
- [30] S. Jetter, D. Dwyer, W.-Q. Jiang, D.-W. Liu, Y.-F. Wang, Z.-M. Wang et al., *PMT waveform modeling at the Daya Bay experiment*, *Chin. Phys. C* **36** (2012) 733.
- [31] Y. Huang et al., *The Flash ADC system and PMT waveform reconstruction for the Daya Bay Experiment*, *Nucl. Instrum. Meth. A* **895** (2018) 48 [1707.03699].
- [32] G.-h. Huang, W. Jiang, L.-j. Wen, Y.-f. Wang and W.-M. Luo, *Data-driven simultaneous vertex and energy reconstruction for large liquid scintillator detectors*, *Nucl. Sci. Tech.* **34** (2023) 83 [2211.16768].
- [33] J.J. Cowan, F.-K. Thielemann and J.W. Truran, *The R-process and nucleochronology*, *Phys. Rept.* **208** (1991) 267.
- [34] “National nuclear data center.” <https://www.nndc.bnl.gov/>.
- [35] “IAEA nuclear data services.” <https://www-nds.iaea.org/>.
- [36] JUNO collaboration, *Sub-percent precision measurement of neutrino oscillation parameters with JUNO*, *Chin. Phys. C* **46** (2022) 123001 [2204.13249].
- [37] JUNO collaboration, *Radioactivity control strategy for the JUNO detector*, *JHEP* **11** (2021) 102 [2107.03669].
- [38] J. Zhao, Z.-Y. Yu, J.-L. Liu, X.-B. Li, F.-H. Zhang and D.-M. Xia, *$^{13}\text{C}(\alpha, n)^{16}\text{O}$ background in a liquid scintillator based neutrino experiment*, *Chin. Phys. C* **38** (2014) 116201 [1312.6347].
- [39] V.A. Kudryavtsev, *Muon simulation codes MUSIC and MUSUN for underground physics*, *Comput. Phys. Commun.* **180** (2009) 339 [0810.4635].
- [40] KamLAND collaboration, *Production of Radioactive Isotopes through Cosmic Muon Spallation in KamLAND*, *Phys. Rev. C* **81** (2010) 025807 [0907.0066].
- [41] Borexino collaboration, *Measurement of the solar 8B neutrino rate with a liquid scintillator target and 3 MeV energy threshold in the Borexino detector*, *Phys. Rev. D* **82** (2010) 033006 [0808.2868].
- [42] JUNO collaboration, *Prospects for detecting the diffuse supernova neutrino background with JUNO*, *JCAP* **10** (2022) 033 [2205.08830].
- [43] G. Battistoni, A. Ferrari, T. Montaruli and P.R. Sala, *The atmospheric neutrino flux below 100-MeV: The FLUKA results*, *Astropart. Phys.* **23** (2005) 526.

- [44] KamLAND collaboration, *A study of extraterrestrial antineutrino sources with the KamLAND detector*, *Astrophys. J.* **745** (2012) 193 [[1105.3516](#)].
- [45] R. Möllenberg, F. von Feilitzsch, D. Hellgartner, L. Oberauer, M. Tippmann, V. Zimmer et al., *Detecting the Diffuse Supernova Neutrino Background with LENA*, *Phys. Rev. D* **91** (2015) 032005 [[1409.2240](#)].
- [46] C. Andreopoulos, C. Barry, S. Dytman, H. Gallagher, T. Golan, R. Hatcher et al., *The GENIE Neutrino Monte Carlo Generator: Physics and User Manual*, [1510.05494](#).
- [47] T. Golan, J.T. Sobczyk and J. Zmuda, *NuWro: the Wroclaw Monte Carlo Generator of Neutrino Interactions*, *Nucl. Phys. B Proc. Suppl.* **229-232** (2012) 499.
- [48] M. Honda, M. Sajjad Athar, T. Kajita, K. Kasahara and S. Midorikawa, *Atmospheric neutrino flux calculation using the NRLMSISE-00 atmospheric model*, *Phys. Rev. D* **92** (2015) 023004 [[1502.03916](#)].
- [49] A.J. Koning and D. Rochman, *Modern Nuclear Data Evaluation with the TALYS Code System*, *Nucl. Data Sheets* **113** (2012) 2841.
- [50] J. Cheng, Y.-F. Li, L.-J. Wen and S. Zhou, *Neutral-current background induced by atmospheric neutrinos at large liquid-scintillator detectors: I. model predictions*, *Phys. Rev. D* **103** (2021) 053001 [[2008.04633](#)].
- [51] JUNO collaboration, *Feasibility and physics potential of detecting ^8B solar neutrinos at JUNO*, *Chin. Phys. C* **45** (2021) 023004 [[2006.11760](#)].
- [52] D. Dörflinger, L. Wallner, L. Oberauer, A. Steiger, M.R. Stock, U. Fahrenholz et al., *Measuring the fluorescence time profile of the juno liquid scintillator using gamma radiation and a pulsed neutron beam*, *Zenodo* (2020) .
- [53] J. Cheng, X.-J. Luo, G.-S. Li, Y.-F. Li, Z.-P. Li, H.-Q. Lu et al., *Pulse shape discrimination technique for diffuse supernova neutrino background search with JUNO*, [2311.16550](#).
- [54] G.J. Feldman and R.D. Cousins, *A Unified approach to the classical statistical analysis of small signals*, *Phys. Rev. D* **57** (1998) 3873 [[physics/9711021](#)].
- [55] J.J. Gomez-Cadenas, J. Martin-Albo, M. Sorel, P. Ferrario, F. Monrabal, J. Munoz-Vidal et al., *Sense and sensitivity of double beta decay experiments*, *JCAP* **06** (2011) 007 [[1010.5112](#)].
- [56] J. Conrad, O. Botner, A. Hallgren and C. Perez de los Heros, *Including systematic uncertainties in confidence interval construction for Poisson statistics*, *Phys. Rev. D* **67** (2003) 012002 [[hep-ex/0202013](#)].